Journal of Photochemistry & Photobiology, A: Chemistry 453 (2024) 115680

Contents lists available at ScienceDirect

Journal of Photochemistry & Photobiology, A: Chemistry

journal homepage: www.elsevier.com/locate/jphotochem

Probing multifunctional applications of $LiCa_2Mg_2V_3O_{12}$: Sm^{3+} phosphor using Judd-Ofelt analysis and dual mode non-contact optical thermometry

R. Raji [a], P.S. Anjana [b], N. Gopakumar [a,*]

[a] PG Department of Physics and Research Centre, Mahatma Gandhi College, University of Kerala, Thiruvananthapuram, Kerala 695004, India
[b] PG Department of Physics, All Saints' College, University of Kerala, Thiruvananthapuram, Kerala 695007, India

ARTICLE INFO

Keywords:
Vanadate
Judd-Ofelt analysis
Non-contact optical thermometry
Thermochromic phosphor

ABSTRACT

$LiCa_2Mg_2V_3O_{12}$:Sm^{3+} phosphors have been prepared by solid state method and analysed by X-ray diffraction, EDX-elemental mapping, UV–VIS-NIR spectroscopy, photoluminescence (PL) and temperature dependent photoluminescence (TDPL). The absorption spectra analysis using Judd-Ofelt theory provides the intensity parameters and manifest the covalent nature of Sm-O bond. The PL spectra monitored at 338 nm excitation exhibits emission peaks of Sm^{3+} at 567, 617 and 651 nm in addition to the broad band emission of $LiCa_2Mg_2V_3O_{12}$ host. The Commision Internationale deL'Eclairage (CIE) coordinates, correlated color temperature (CCT) and color rendering index (CRI) values elucidate the efficient yellow emission of phosphors. The radiative parameters are evaluated and have outrageous branching ratio and cross section that aids in visible laser applications. The optical thermometry of phosphor is carried out by utilizing FIR method through selecting spectral modes $^6H_{5/2}$/ VO_4^{3-}, $^6H_{7/2}$/VO_4^{3-} and $^6H_{9/2}$/ VO_4^{3-}. The mode $^6H_{9/2}$/ VO_4^{3-} have higher absolute sensitivity (S_a) and relative sensitivity (S_r) values of 0.4418 K^{-1} and 1.6079% K^{-1}. The temperature resolution of modes are 0.1633, 0.1677 and 0.1563 K respectively. The thermochromic study reveals the high chromaticity shift ($\Delta s = 0.1869$) of phosphor and the $S_a(x)$ and $S_r(x)$ values evaluated based on CIE coordinates are 0.0011 K^{-1} and 0.2407% K^{-1} respectively. The PL and TDPL characteristics of prepared phosphor suggest that it have multifunctional application in the fields of lasers, thermo-sensors, thermochromic displays and LEDs.

1. Introduction

The precise measurement of temperature is essential in daily life as it have crucial role in the fields of agriculture production, industrial manufacture, medical diagnosis and scientific research [1–4]. The demand for non-contact optical thermometers has upsurge after the outburst of Covid-19 pandemic in 2019 [5]. The non-contact optical thermometers have advantages over other methods owing to its efficient determination of temperature in harsh, fast-moving and corrosive environments [2]. Furthermore, non-contact optical thermometers exhibit fast response, high accuracy and marked sensitivity that aids in optimum evaluation of temperature [12].

The detection of temperature is realized through temperature sensitive parameters such as emission intensity, Commision Internationale deL'Eclairage coordinates, flourescence intensity ratio, flourescence lifetime and excitation intensity ratio [1 6,7]. Among them, the thermometers based on fluorescence intensity ratio (FIR) is more adaptable due to their inherent advantages [2 7–11]. In FIR method the thermally coupled energy level (TCEL) emissions from rare earth elements Nd, Ho, Er etc. are utilized to analyze the thermo sensing properties [12,13]. However, the constant energy difference of thermally coupled levels limits their sensitivity. Along with this, the inverse dependence of relative sensitivity (S_r) on square of temperature constraints temperature measurement at high temperatures [2,14]. To overcome this, researchers developed FIR thermometer based on dual luminescent centers [15,16]. Rare earth activated fluorescent materials exhibit dual luminescent centers and have higher S_a and S_r values than those based on TCELs [1,14,17].

It is noteworthy that the selection of host material has significant role in luminescence characteristics of rare earth (RE) activated systems. Vanadate is a versatile material which exhibit intense emission in visible region and strong absorption in UV region. On doping vanadate host with rare earth ions, the phonon assisted energy transfer from vanadate group to rare earth ion occurs. Also, the emission from both vanadate host and rare earth ion appears simultaneously [18]. Thus, rare earth activated vanadate system can be efficiently employed for the

---

* Corresponding author.
E-mail address: gopkumar.n@gmail.com (N. Gopakumar).

https://doi.org/10.1016/j.jphotochem.2024.115680
Received 9 January 2024; Received in revised form 26 March 2024; Accepted 12 April 2024

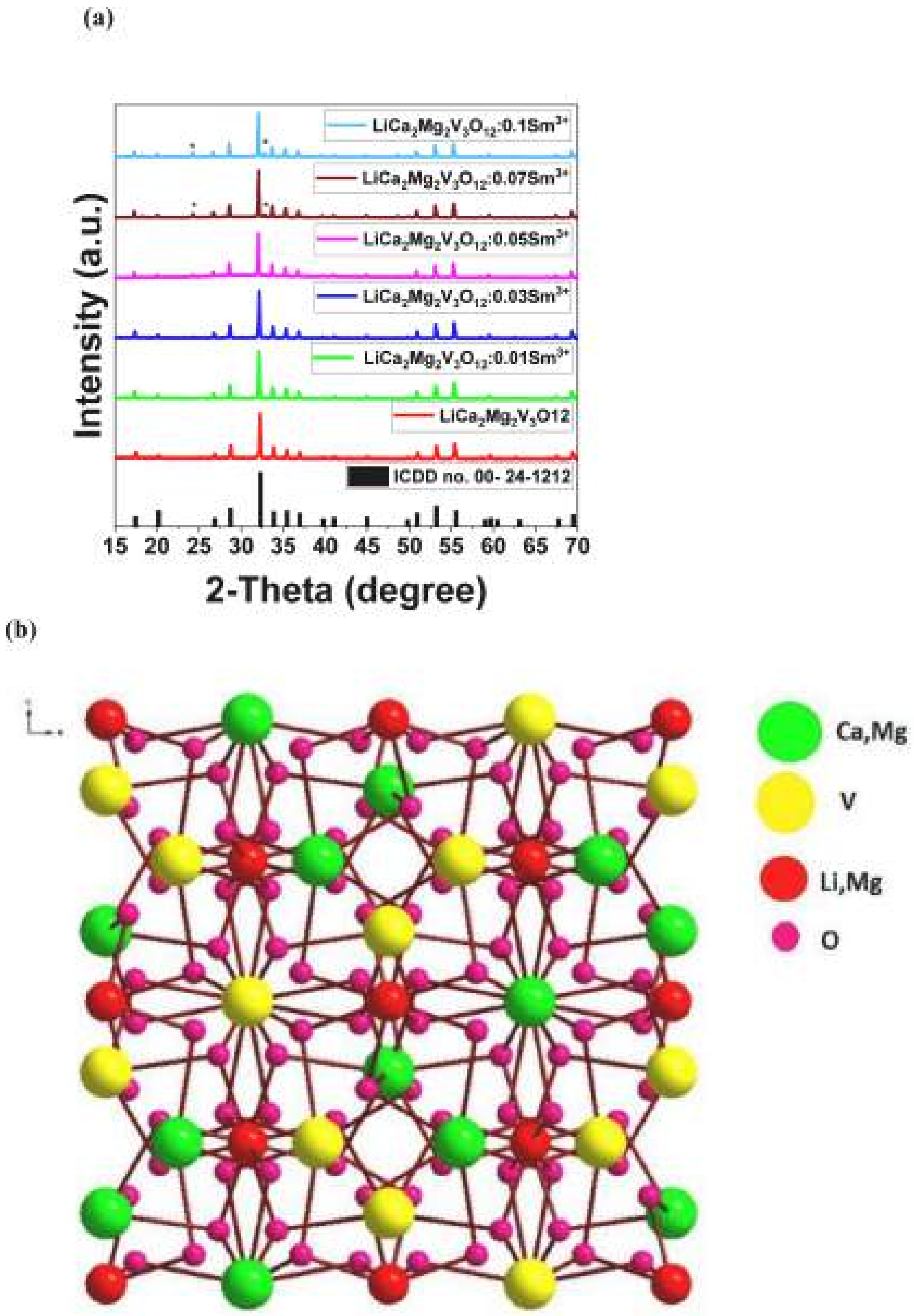

Fig. 1. **(a)** PXRD of $LiCa_2Mg_2V_3O_{12}$:xSm^{3+} phosphors and **(b)** Crystal structure of $LiCa_2Mg_2V_3O_{12}$.

estimation of fluorescence intensity ratio [12]. Literature review shows very few reports regarding fluorescence intensity ratio and sensitivity measurments using different spectral modes. The spectral mode selection is a convenient method to obtain ultra high sensitivity [12]. Hence, optical thermometry studies based on spectral mode selection need more attentention and is need of the time.

In this present study, $LiCa_2Mg_2V_3O_{12}$ host is selected for the doping of rare earth element samarium. The $LiCa_2Mg_2V_3O_{12}$ has green emission and introducing orange-red emission of samarium into host results in tunable emission [12]. As far as we know there are no reports regarding

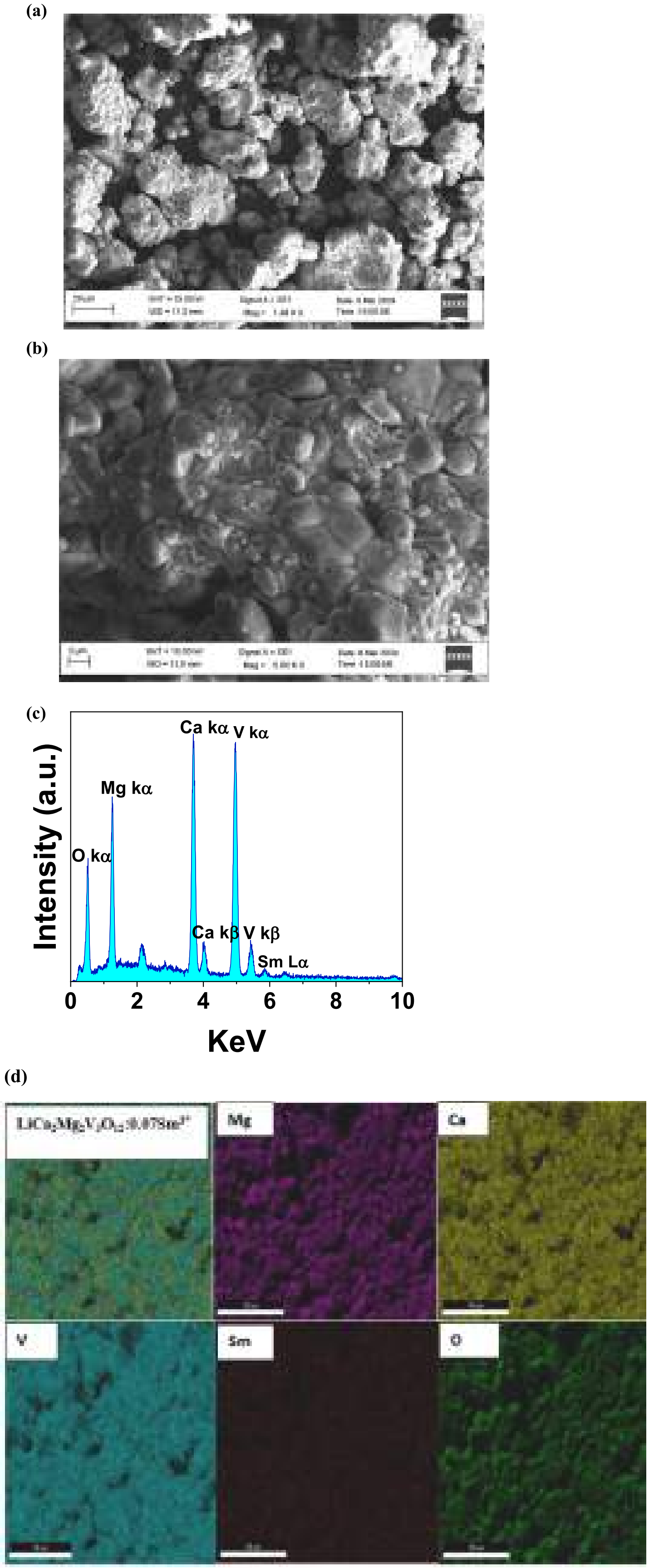

Fig. 2. SEM images of $LiCa_2Mg_2V_3O_{12}$:0.07Sm^{3+} phosphor at (a) low magnification (b) high magnification (c) EDX spectra and (d) elemental mapping.

the optical and luminescence properties of Sm^{3+} doped $LiCa_2Mg_2V_3O_{12}$ phosphors. Herein, we synthesized novel $LiCa_2Mg_2V_3O_{12}$:Sm^{3+} phosphors *via* solid state method. Their structural and optical properties are studied in detail. The radiative parameters are assessed through Judd-Ofelt theory. The thermo sensing activity is analysed by FIR method through spectral mode selection between VO_4^{3-} and Sm^{3+} emission. The thermochromics properties of phosphors on the basis of CIE coordinates are discussed.

2. Experimental

2.1. Synthesis method

A series of $LiCa_2Mg_2V_3O_{12}$:Sm^{3+} (x = 0, 0.01, 0.03, 0.05, 0.07 and 0.1) phosphors were synthesized by solid-state reaction route. The stoichiometric amounts of $CaCO_3$ (Sigma Aldrich)$_,$ Li_2CO_3 (Sigma Aldrich), $(MgCO_3)_4$ •Mg $(OH)_2{\cdot}5H_2O$ (Sigma Aldrich), V_2O_5 (Sigma Aldrich) and Sm_2O_3 (Sigma Aldrich) were accurately weighed and mixed using an agate mortar for two hours in acetone medium. They were then transferred into alumina crucibles and calcined at 800°C for 3 h. The calcined products were furnace cooled to room temperature and then ground for further characterizations.

2.2. Characterization

The crystal phase of phosphors was identified by powder X-ray diffractometer (D8 Advanced Bruker) with Ni-filtered Cu-Kα (λ = 1.5406 Å). The morphology and elemental composition of the phosphor were studied using energy dispersive X-ray spectrometer (Carl Zeiss EVO 18 Research). The UV–Vis-NIR absorption spectra and diffuse reflectance spectra of phosphors were measured using Agilent Cary-5000 UV–Vis-NIR spectrophotometer with integrating sphere attachment. The photoluminescence excitation, emission and decay lifetime of the phosphors were analyzed using Horiba Jobin Yvon Flourolog III. The quantum efficiency and temperature dependent PL spectrum of the phosphor were studied by EDINBURGH FLS 1000 Fluorescence Spectrometer. The CIE, CCT and CRI values were calculated from emission spectra using color calculator software (OSRAM SYLVANIA).

3. Results and discussion

3.1. Crystal structure

The powder X-ray diffraction analysis (PXRD) is used to examine the structure and phase purity of prepared phosphors. The PXRD pattern of $LiCa_2Mg_2V_3O_{12}$:xSm^{3+} (x = 0, 0.01, 0.03, 0.05, 0.07 and 0.1) phosphors, as well as the ICDD card of isostructural $Ca_3LiMgV_3O_{12}$ (ICDD no. 00–24-1212) are depicted in Fig. 1 **(a)**. The patterns are well indexed to cubic garnet structure with *Ia-3d* (2 3 0) space group. When the Sm^{3+} content is elevated to 5 mol%, some impurity peaks are detected at 24.24° and 32.73° corresponding to the $SmVO_4$ phase (ICDD no. 00–17-0876) [19]. The phase fraction of 7 mol% and 10 mol% of Sm^{3+} doped $LiCa_2Mg_2V_3O_{12}$ phosphors are estimated based on emission intensity and found to be 1.99% and 2.10% respectively. The appearance of impurity peaks manifests the solubility limitation of Sm^{3+} ion in $LiCa_2Mg_2V_3O_{12}$ host [20].

The ionic radius of Sm^{3+} (1.079 Å) is very close to Ca^{2+} (1.12 Å) and hence the Sm^{3+} ions are intended to replace the Ca^{2+} ion [6]. The radius percentage difference (D_r) between the doped ion and replaced ion can be calculated using the expression given by Pires and Davlos and it should be less than 30%. The D_r value is determined by Eq. (1) [15]:

$$D_r = 100\% \times \frac{R_{m(C.N)} - R_{d(C.N)}}{R_{m(C.N)}} \tag{1}$$

where *C.N* is the coordination number, $R_{m(C.N)} and R_{d(C.N)}$ are the ionic radii of replaced ion and dopant ion respectively. For coordination number 8, the D_r values between the cations and Sm^{3+} ion are 3.66%, 41.97%, 49.86% and 199% for Ca^{2+}, Li^{+}, Mg^{2+} and V^{5+} respectively. It is evident that the Sm^{3+} ion can simply substitute Ca^{2+} cation.

Table 1

EDX spectra analysis of $LiCa_2Mg_2V_3O_{12}$:$0.07Sm^{3+}$ phosphor.

Element	Energy (KeV)	Atomic %
Ca	3.69	14.10
Mg	1.25	15.37
V	4.96	19.02
O	0.52	50.94
Sm	5.85	0.56

Fig. 1**(b)** shows the simulated crystal structure of $LiCa_2Mg_2V_3O_{12}$ based on the generated crystallographic information file (CIF). The lattice parameters of cubic garnet (Ia-3d space group) $LiCa_2Mg_2V_3O_{12}$ phosphor are $a = b = c = 12.3967$ Å, $\alpha = \beta = \gamma = 90^\circ$ and $Z = 8$. The Ca^{2+} ions and one Mg^{2+} ion both occupies the $[CaO_8/MgO_8]$ 8-fold dodecahedron. The Li^{+} ion and other Mg^{2+} are in 6-fold octahedron. The sites of V^{5+} surround four oxygen to form tetrahedron unit [21].

The scanning electron microscope (SEM) images of $LiCa_2Mg_2V_3O_{12}$:$0.07Sm^{3+}$ phosphor at different magnifications are shown in Fig. 2 **(a)** & **(b)**. The particle size of phosphor ranges from 2 to 8 μm.

The elemental composition of the phosphor is determined by EDX analysis as shown in Fig. 2 **(c)**. The distribution displays the characteristic energy peaks of Ca, Mg, V, O and Sm^{3+} present in $LiCa_2Mg_2V_3O_{12}$:$0.07Sm^{3+}$ phosphor. As Li have lighter molar mass, it is undetectable in EDX spectra. The energy values and atomic percentage of constituent elements are presented in Table 1. Since, the presence of Li is undetectable, the cation ratio of Ca/Mg/V is used to verify the atomic percentage of the compound. The cation ratio of Ca/Mg/V based on atomic percentage is 2.01:2.19:2.71 and is close to the theoretical cation ratio 2:2:3.

It is obvious that the EDX spectra confirms the elemental composition of phosphor [18]. Fig. 2 **(d)** shows the elemental mapping of $LiCa_2Mg_2V_3O_{12}$:$0.07Sm^{3+}$ phosphor. The elemental mapping reveals the uniform distribution of constituent elements on the outer surface of phosphor. The light and dark areas in the image manifests the uneven height of phosphor powder during the test. The individual color diagrams exhibit the spots of opposite elements presented in different colors against a dark background. The overall uniform distribution of the elements validates the effective incorporation of Sm^{3+} ion into $LiCa_2Mg_2V_3O_{12}$ host.

3.2. Optical properties

The UV–Visible-NIR spectra of $LiCa_2Mg_2V_3O_{12}$:xSm^{3+} (x = 0.01, 0.03, 0.05, 0.07 and 0.1) phosphors are shown in Fig. 3 **(a)**. The inset of Fig. 3**(a)** shows the UV–Visible-NIR spectra of $LiCa_2Mg_2V_3O_{12}$ host. The broad band UV absorption spectrum is due to the charge transfer transition of $O^{2-} \rightarrow V^{5+}$. The sharp peaks present in the visible and NIR region at wavelength of 467, 476, 480, 954, 1095, 1262, 1413, 1538, 1583 and 1944 nm are ascribed to the absorption transitions of Sm^{3+} from $^6H_{5/2}$ ground level to $^4I_{13/2}$, $^4I_{11/2}$, $^4M_{15/2}$, $^6F_{11/2}$, $^6F_{9/2}$, $^6F_{7/2}$, $^6F_{5/2}$, $^6F_{3/2}$, $^6F_{1/2}$ and $^6H_{13/2}$ respectively [22]. In order to understand the bonding behaviour of Sm^{3+} ion, the nephelauxetic ratio (β) and the bonding parameter (δ) can be calculated using the following equations [23,24]:

$$\beta = \frac{\nu_c}{\nu_a} \tag{2}$$

where ν_c and ν_a are the band positions of $LiCa_2Mg_2V_3O_{12}$:Sm^{3+} host and aqueous solution in cm^{-1}.

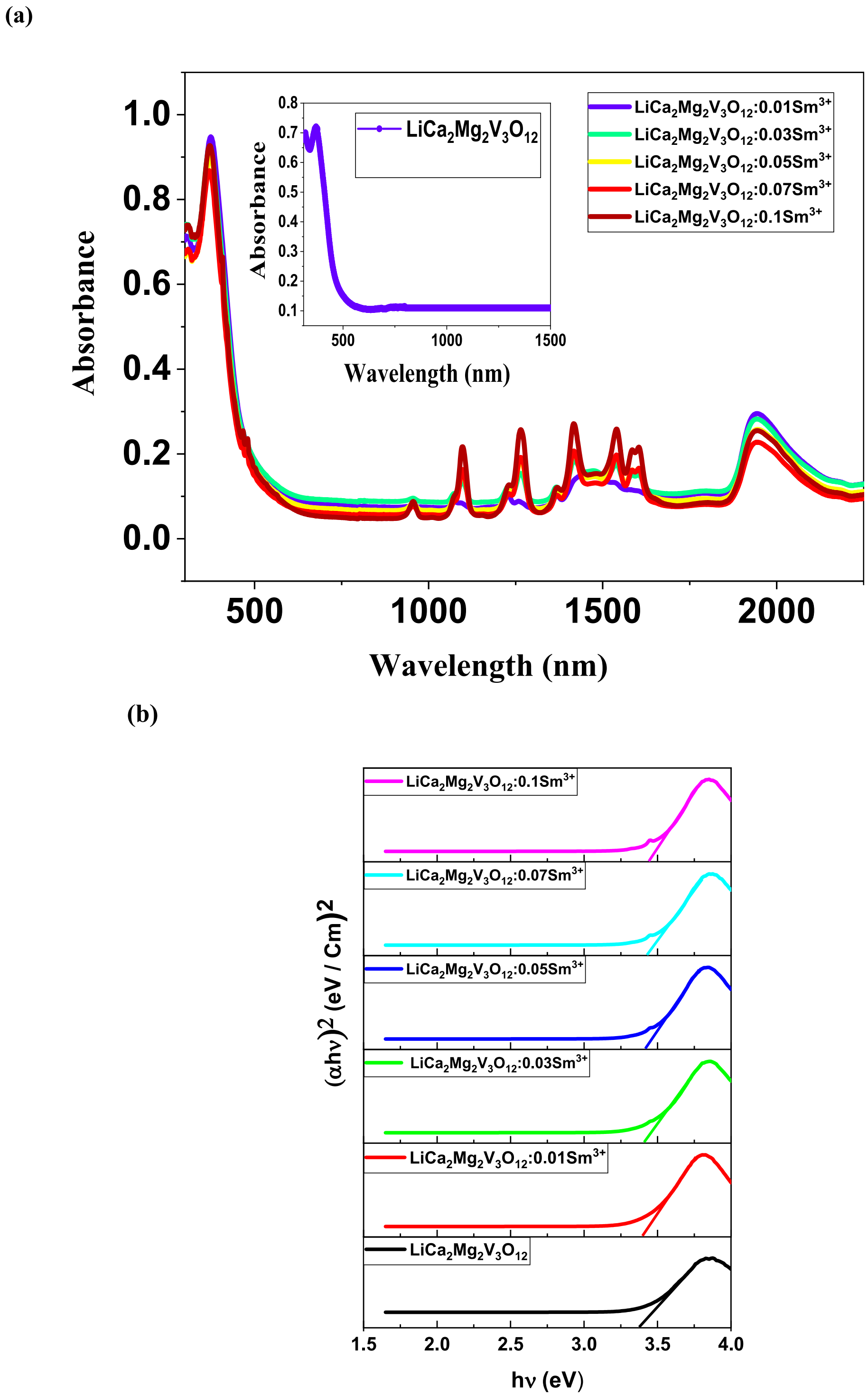

Fig. 3. **(a)** UV–Vis-NIR spectra **(b)** DRS spectra and **(c)** Tauc plot of LiCa$_2$Mg$_2$V$_3$O$_{12}$:xSm^{3+} phosphors.

$$\delta = \frac{1-\overline{\beta}}{\overline{\beta}} \times 100 \tag{3}$$

where $\overline{\beta}$ is the average nephelauxetic ratio. The calculated values of nephelauxetic ratio and bonding parameter are tabulated in Table 2. The positive value of δ implies covalent nature of Sm^{3+} ion in LiCa$_2$Mg$_2$V$_3$O$_{12}$ host.

The bandgap energy (E_g) of phosphors is obtained by applying Tauc analysis. The plot of $(\alpha h\nu)^2$ versus photon energy ($h\,\nu$) is shown in Fig. 3 **(b)**. The energy gap (E_g) is evaluated using the expression [20]:

$$(\alpha h\nu)^n = A\left(h\nu - E_g\right) \tag{4}$$

where hν is the photon energy, α is the absorption coefficient, A is the absorption constant and $n = 2$ for direct transition.

The band gap energy of LiCa$_2$Mg$_2$V$_3$O$_{12}$:xSm^{3+} (x = 0, 0.01, 0.03, 0.05, 0.07 and 0.1) phosphors are observed to be 3.36, 3.39, 3.40, 3.41, 3.43 and 3.44 eV. As the dopant concentration increases the bandgap energy also broaden, this can be described by Burstein Moss effect. On doping, the donor electrons occupies the bottom level of conduction band, as a consequence of this the Fermi levels shifts towards the

Table 2

Nephelauxetic ratio and bonding parameter of $LiCa_2Mg_2V_3O_{12}$:Sm^{3+} phosphor.

Sl.No.	$^6H_{5/2} \rightarrow$	ν_c (cm^{-1})	ν_a (cm^{-1})	β
1	$^4I_{13/2}$	21,413	21,600	0.9913
2	$^4I_{11/2}$	21,008	21,100	0.9956
3	$^4M_{15/2}$	20,833	20,800	1.0015
4	$^6F_{11/2}$	10,482	10,500	0.9982
5	$^6F_{9/2}$	9132	9200	0.9926
6	$^6F_{7/2}$	7923	8000	0.9903
7	$^6F_{5/2}$	7077	7100	0.9967
8	$^6F_{3/2}$	6501	6630	0.9805
9	$^6F_{1/2}$	6317	6400	0.9870
10	$^6H_{13/2}$	5144	5000	1.0288
$\bar{\beta} = 0.9962$, $\delta = 0.0038$ (covalent bonding)				

Table 3

Comparison table of bandgap values.

Compound	Bandgap (eV)	Ref.
$LiCa_3MgV_3O_{12}$	3.46	[18]
$LiCa_3ZnV_3O_{12}$	3.40	[18]
$Ca_3LiMgV_3O_{12}$:Eu^{3+}	3.50	[20]
$LiCa_2Mg_2V_3O_{12}$:Dy^{3+}	3.42	[26]

Table 5

J-O intensity parameters Ω_2, Ω_4, Ω_6 and spectroscopic quality factor (χ) of phosphors.

Sm^{3+} concentration (mol%)	Judd-Ofelt intensity parameters			χ
	Ω_2 ($\times10^{-20}$cm^2)	Ω_4 ($\times10^{-20}$cm^2)	Ω_6 ($\times10^{-20}$cm^2)	
0.01	3.6175	3.1585	3.1118	1.0150
0.03	4.2113	3.9709	3.7029	1.0723
0.05	4.8520	4.6083	4.1653	1.1063
0.07	5.6124	5.3183	4.7606	1.1171
0.1	7.2392	6.5501	5.3858	1.2161

Table 6

Comparison of Ω_2, Ω_4, Ω_6 and χ values of phosphor with previously reported materials.

Phosphor	Ω_2($\times10^{-20}$cm^2)	Ω_4 ($\times10^{-20}$cm^2)	Ω_6 ($\times10^{-20}$cm^2)	Ref.
LaOCl:Sm^{3+}	0.4081	0.4842	0.615	[31]
SKBL:Sm^{3+} glass	2.81	3.05	1.52	[34]
$Sr_{0.5}Ca_{0.5}TiO_3$:Sm^{3+}	0.5077	0.3206	0.2411	[33]
ZPAB: Sm^{3+} glass	2.36	4.84	2.51	[35]
$La_{2-x}Sm_x(MoO_4)_3$	1.1441	0.0523	0.0522	[22]
$LiCa_2Mg_2V_3O_{12}$: xSm^{3+}	7.2392	6.5501	5.3858	Present work

conduction band. The partial filling of conduction band thus blocks the lower levels and broadens the bandgap of phosphor. The photon excitation energy of phosphors is 3.66 eV (338 nm) and is greater than the bandgap energy of phosphors. The intense emission in phosphors can be produced by the effective excitation energy that is greater than the bandgap energy. Also, the band gap values are comparable to other vanadate garnet phosphors which shows efficient emission (Table 3). The relation connecting bandgap energy and refractive index is given by Dimithrov-Sakka relation and is expressed as follows [23,24]:

$$\frac{(n^2-1)}{(n^2+2)} = 1 - \sqrt{\frac{E_g}{20}} \tag{5}$$

where, n corresponds to the refractive index and E_g is the bandgap energy. The refractive index values of $LiCa_2Mg_2V_3O_{12}$:xSm^{3+} (x = 0.01, 0.03, 0.05, 0.07 and 0.1) phosphors are 2.2993, 2.2969, 2.2946, 2.2900 and 2.2877 respectively. The calculated values of refractive index are employed for the calculation of Judd-Ofelt intensity parameters.

The Judd-Ofelt (J-O) theory is an effective tool to analyse the radiative transitions of rare earth ions in various coordination environments. The analysis is also used to examine the site symmetry and bond covalency between metal ion and ligand. The J-O analysis depends on the accurate measurements based on integrated absorption cross-section. The line strength using the integrated absorption cross section is given by [25]:

$$S_{meas} = \frac{3hc(2J+1)}{8\pi^3 e^2 \bar{\lambda}} n \left(\frac{3}{n^2+2}\right)^2 \int \sigma(\lambda) d\lambda \tag{6}$$

where J is the total angular momentum of initial state, $\bar{\lambda}$ is the mean wavelength of a particular absorption transition, n corresponds to the refractive index of host material and $\int \sigma(\lambda) d\lambda$ is the value of integrated absorption cross-section. The absorption cross-section $\sigma(\lambda)$ is evaluated using the relation:

$$\sigma(\lambda) = \frac{2.303^{*}A}{tN} \tag{7}$$

where A is the absorbance, t is the thickness of sample and is taken as 1 mm and N corresponds to the Sm^{3+} ion concentration/cm^3. The line strength of electric dipole transition between initial $|(S,L)J\rangle$ and final $|(S',L')J'\rangle$ state can be obtained by J-O theory using following expression:

$$S_{cal} = \sum_{\lambda=2,4,6} \Omega_\lambda \left| \langle (S,L)J \| U^{(\lambda)} \| (S',L')J' \rangle \right|^2 \tag{8}$$

where $\|U^{(\lambda)}\|$ is the doubly reduced matrix elements of unit tensor operator with rank $\lambda = 2, 4, 6$. The values of $\|U^{(\lambda)}\|$ are obtained from literature reported by Carnall et al [27]. The Judd-Ofelt parameters Ω_2, Ω_4 and Ω_6 are determined by using least square fitting between measured and calculated line strength [25]. Table 4 shows the values of measured line strength (S_{meas}), calculated line strength (S_{cal}) and root mean square deviation (σ) of $LiCa_2Mg_2V_3O_{12}$:xSm^{3+} (x = 0, 0.01, 0.03, 0.05, 0.07 and 0.1) phosphors. The lower value of σ signifies better fitting between S_{meas} and S_{cal} values and further, it confirms the validity of J-O parameters.

The estimated values of J-O intensity parameters Ω_2, Ω_4, Ω_6 and spectroscopic quality factor (χ) of phosphors are tabulated in Table 5.

Table 4

Values of measured line strength ($\times10^{-20}$ cm^2), calculated line strength ($\times10^{-20}$ cm^2) and root mean square deviation ($\times10^{-20}$ cm^2) of $LiCa_2Mg_2V_3O_{12}$:xSm^{3+} (x = 0.01, 0.03, 0.05, 0.07 and 0.1) phosphors.

$^6H_{5/2} \rightarrow$	0.01Sm^{3+}		0.03Sm^{3+}		0.05Sm^{3+}		0.07Sm^{3+}		0.1Sm^{3+}	
	S_{meas}	S_{cal}	S_{meas}	S_{cal}	S_{meas}	S_{cal}	S_{meas}	S_{cal}	S_{meas}	S_{cal}
$^6F_{11/2}$	0.653	0.162	0.710	0.193	0.783	0.217	1.172	0.248	1.296	0.281
$^6F_{9/2}$	1.314	1.127	1.475	1.345	1.750	1.516	1.892	1.734	2.255	1.973
$^6F_{7/2}$	1.592	1.799	2.006	2.171	2.210	2.463	2.587	2.823	2.926	3.271
$^6F_{5/2}$	1.132	1.017	1.329	1.267	1.517	1.469	1.738	1.696	2.194	2.100
$^6F_{3/2}$	0.891	0.953	1.162	1.149	1.447	1.329	1.667	1.535	2.041	1.938
$^6F_{1/2}$	0.729	0.701	0.797	0.816	0.846	0.940	0.985	1.088	1.312	1.403
σ	± 0.319		± 0.311		± 0.357		± 0.529		± 0.611	

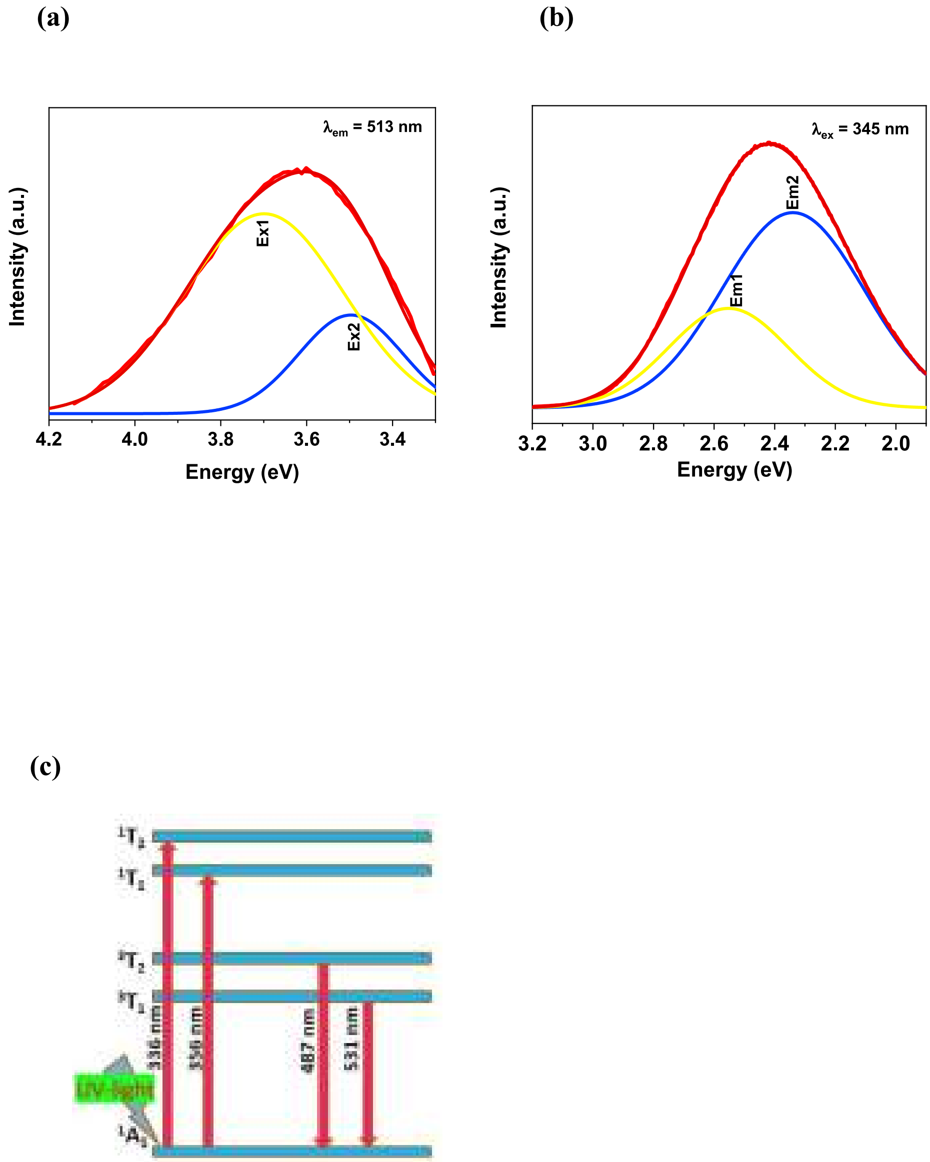

Fig. 4. **(a)** Excitation spectrum **(b)** emission spectrum and **(c)** excitation and emission process in VO_4^{3-} group.

The J-O parameters follows the trend $\Omega_2 > \Omega_4 > \Omega_6$ in Sm^{3+} doped $LiCa_2Mg_2V_3O_{12}$. The higher value of Ω_2 signifies higher asymmetry of Sm^{3+} site in $LiCa_2Mg_2V_3O_{12}$ host lattice and the covalency of Sm-O bonds. The covalency of Sm-O bond is in agreement with the bonding parameter calculations. The Ω_4 and Ω_6 parameters are long range parameters that depend on bulk properties of material such as viscosity, rigidity, basicity and dielectric constant [28,29]. A comparison of Ω_2, Ω_4 and Ω_6 values with reported Sm^{3+} doped materials is given in Table 6 and the higher Ω_2 value of present system manifests higher degree of covalency. The spectroscopic quality factor (χ) of phosphors is calculated using following equation [30]:

$$\chi = \frac{\Omega_4}{\Omega_6} \tag{9}$$

For all concentrations of Sm^{3+} the χ value is greater than one and is comparable with previously reported materials LaOCl:Sm^{3+}[31], LBZnFSm [32], $Sr_{0.5}Ca_{0.5}TiO_3$:Sm^{3+}[33], which implies the practical application of phosphor in optical devices.

3.3. Luminescence properties

To understand the intrinsic luminescence properties of the $LiCa_2Mg_2V_3O_{12}$ host, the PLE and PL spectra are recorded and are shown in Fig. 4**(a)** and **(b)** respectively. The excitation spectra monitored at 513 nm consists of broad band spectra (i.e., 300–380 nm) centred at 345 nm. The spectra can be deconvoluted into two peaks at 3.69 eV (336 nm) and 3.49 eV (356 nm) using Gaussian function. The peaks at 336 and 356 nm corresponding to the transitions $^1A_1 \rightarrow {}^1T_2$ and $^1A_1 \rightarrow {}^1T_1$ are ascribed to the charge transfer transitions of VO_4^{3-} group. The PL spectra of $LiCa_2Mg_2V_3O_{12}$ phosphor recorded at 345 nm consists of broad band emission spectra having central wavelength of 513 nm. The $LiCa_2Mg_2V_3O_{12}$ host has green emission and the emission spectra can be decomposed into two bands by Gaussian function. The deconvoluted sub-bands at 2.55 eV (487 nm) and 2.34 eV (531 nm) are attributed to the $^3T_2 \rightarrow {}^1A_1$ and $^3T_1 \rightarrow {}^1A_1$ transitions of VO_4^{3-} group [12]. The excitation and emission process in VO_4^{3-} group is depicted in Fig. 4 **(c)**.

The luminescence properties of $LiCa_2Mg_2V_3O_{12}$:xSm^{3+} phosphors are explored in detail and are shown in Fig. 5**(a)** and **(b)** respectively. The PLE spectrum recorded at 651 nm exhibits broad band spectra and one sharp peak. The intense broad band spectra ascribed to the

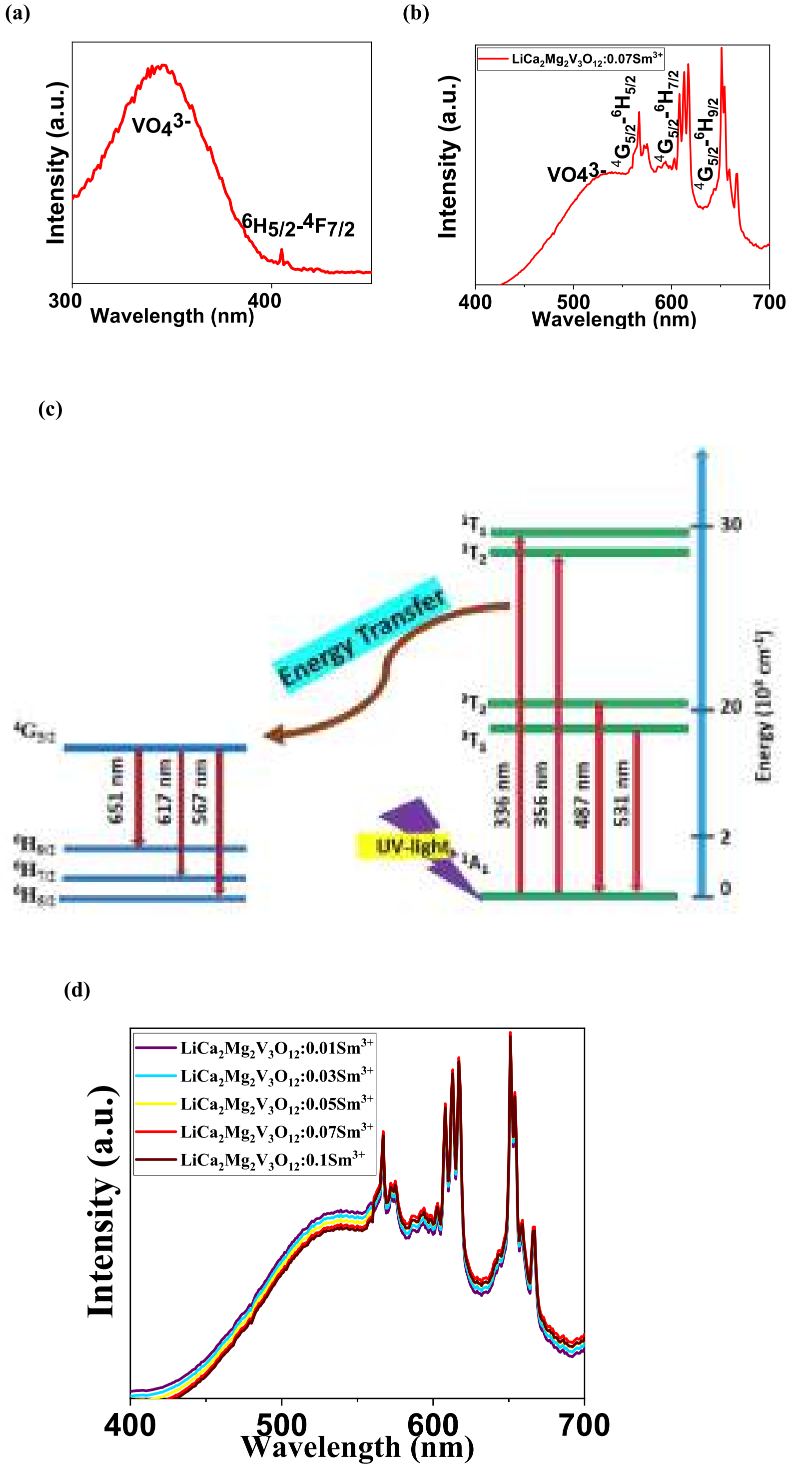

Fig. 5. **(a)** Excitation and **(b)** emission of $LiCa_2Mg_2V_3O_{12}$:$0.07Sm^{3+}$ phosphor **(c)** energy transfer and (d) emission of $LiCa_2Mg_2V_3O_{12}$:xSm^{3+} (x = 0, 0.01, 0.03, 0.05, 0.07 and 0.1) phosphors.

transition of VO_4^{3-} group and the narrow peak at 405 nm ($^6H_{5/2}\rightarrow{}^4F_{7/2}$) originated from the 4f-4f transitions of Sm^{3+} ion. The PL spectra of $LiCa_2Mg_2V_3O_{12}$:$0.01Sm^{3+}$ phosphor monitored at 338 nm exhibits narrow peaks in addition to the broad band emission of VO_4^{3-} group. The peaks at 567, 617 and 651 nm arising from the intra-4f orbital transition of Sm^{3+} ion from $^4G_{5/2}\rightarrow{}^6H_{5/2}$, $^4G_{5/2}\rightarrow{}^6H_{7/2}$ and $^4G_{5/2}\rightarrow{}^6H_{9/2}$ respectively. The photoluminescence results imply that the excitation energy can efficiently transferred from VO_4^{3-} group to the Sm^{3+} ion [5]. The energy level diagram showing the energy transfer process between VO_4^{3-} and Sm^{3+} is shown in Fig. 5**(c)**.

To analyse the optimum dopant concentration of Sm^{3+} ion in $LiCa_2Mg_2V_3O_{12}$ host, a series of $LiCa_2Mg_2V_3O_{12}$:xSm^{3+} (x = 0, 0.01, 0.03, 0.05, 0.07 and 0.1) phosphors are prepared and the corresponding emission spectra at an excitation wavelength of 338 nm is shown in Fig. 5**(d)**. It is observed that all phosphors have identical emission spectra except variation in emission intensity. As the concentration of Sm^{3+} ion increases, the intensity of emission from VO_4^{3-} group decreased and for Sm^{3+} ion the emission initially increases up to 7 mol% and then

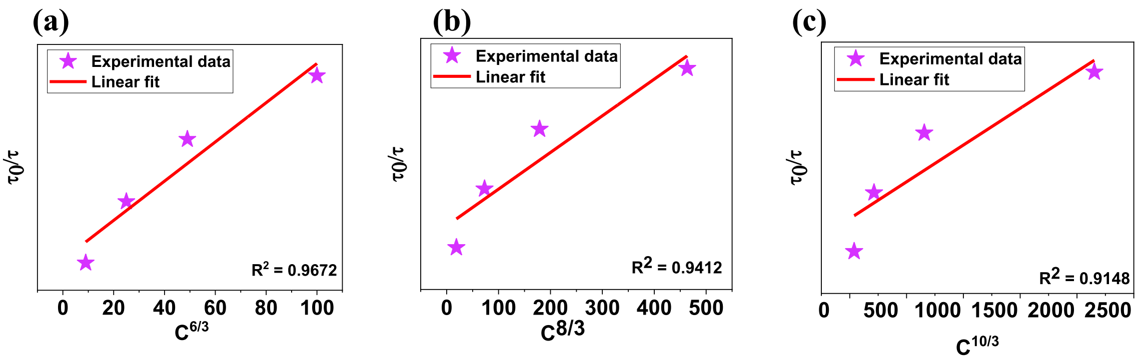

Fig. 6. (a) dipole–dipole (b) dipole-quadrupole and (c) quadrupole–quadrupole interaction mechanism.

decreases. The decrease in emission intensity is due to the concentration quenching effect [5]. In order to determine the concentration quenching mechanism, the critical distance (R_c) is estimated by Blasse relation as follows [21]:

$$R_c = 2\left(\frac{3V}{4\pi X_c N}\right)^{1/3} \tag{10}$$

where unit cell volume $V = 1933.7829$ Å^3, critical concentration $X_c = 0.07$ and number units $N = 8$. The critical distance R_c is found to be 18.7562 Å. The electric multipolar interaction is responsible for the concentration quenching in $LiCa_2Mg_2V_3O_{12}$:Sm^{3+} as the critical distance is greater than 5 Å. The nature of multipolar interaction is evaluated by the equation [36]:

$$\frac{\tau_0}{\tau} = C^{\theta/3} \tag{11}$$

where τ_0 is the intrinsic lifetime, τ is the life time at different concentration of Sm^{3+}, C is the samarium ion concentration and $\theta = 6, 8, 10$. The interaction is dipole–dipole, dipole-quadrupole or quadrupole–quadrupole based on θ values 6, 8 or 10. The different interaction mechanisms are displayed in Fig. 6**(a)–(c)** and the goodness of fit suggest that the concentration quenching is caused by dipole–dipole interaction [36].

The radiative parameters are estimated by incorporating Judd-Ofelt intensity parameters to the emission spectra. The radiative transition probability (A_R) from excited state J' to lower state J is given by [25]:

$$A_{R(J'\rightarrow J)} = A_{ed}+A_{md} = \frac{64\pi^4}{3h\lambda^3(2J+1)}\left[\frac{n(n^2+2)^2}{9}S_{ed}+n^3S_{md}\right] \tag{12}$$

where A_{ed} and A_{md} are the electric and magnetic dipole transition probability respectively. The electric dipole line strength (S_{ed}) and magnetic dipole strength (S_{md}) are evaluated by following expressions:

$$S_{ed} = e^2\sum_{t=2,4,6}\Omega_t\left|\langle(S,L)J\|U^{(t)}\|(S',L')J'\rangle\right|^2 \tag{13}$$

$S_{md} = \mu_B^2|\langle(S,L)J\|L+2S\|(S',L')J'\rangle|^2$; (14) where$\mu_B = \frac{h}{4\pi mc}$. The total radiative transition probability $\sum A_R(J'\rightarrow J)$ is determined by taking sum of radiative transition probability of each transition of Sm^{3+}. The reciprocal of total radiative transition probability gives the radiative life time (τ_{rad}). In accordance with transition probability (A_R), the radiative life time (τ_{rad}) and branching ratio (β_R) are calculated using equations:

$$\tau_{rad} = \frac{1}{\sum A_R(J'\rightarrow J)} \tag{15}$$

$$\beta_R = \frac{A_R(J'\rightarrow J)}{\sum A_R(J'\rightarrow J)} \tag{16}$$

Table 7
Radiative parameters of $LiCa_2Mg_2V_3O_{12}$:xSm^{3+} phosphors.

Concentration	Radiative properties	$^4G_{5/2}\rightarrow{}^6H_{5/2}$	$^4G_{5/2}\rightarrow{}^6H_{7/2}$	$^4G_{5/2}\rightarrow{}^6H_{9/2}$
$0.01Sm^{3+}$	λ_p(nm)	567	617	651
	A_R (s^{-1})	73.23	419.89	401.76
	β_R (Radiative)	0.08183	0.4692	0.4489
	β_R (Experimental)	0.2570	0.2740	0.4689
	σ_e ($\times10^{-22}cm^2$)	0.8044	10.42	11.873
	$\sigma_e \times \Delta\lambda_{eff}$ ($\times10^{-28}$ cm^3)	1.89	1.52	1.81
	$\sigma_e \times \tau_{rad}$ ($\times10^{-25}$ cm^2 s)	0.8993	11.64	13.27
$0.03Sm^{3+}$	λ_p(nm)	567	617	651
	A_R (s^{-1})	78.87	503.46	478.37
	β_R (Radiative)	0.07435	0.4746	0.4509
	β_R (Experimental)	0.2344	0.2928	0.4726
	σ_e ($\times10^{-22}cm^2$)	0.7563	13.38	31.53
	$\sigma_e \times \Delta\lambda_{eff}$ ($\times10^{-28}$ cm^3)	2.04	1.83	2.15
	$\sigma_e \times \tau_{rad}$ ($\times10^{-25}$ cm^2 s)	0.7129	12.61	29.72
$0.05Sm^{3+}$	λ_p(nm)	567	617	651
	A_R (s^{-1})	83.76	568.12	549.15
	β_R (Radiative)	0.0697	0.4730	0.4572
	β_R (Experimental)	0.2196	0.2918	0.4884
	σ_e ($\times10^{-22}cm^2$)	0.6681	15.08	35.87
	$\sigma_e \times \Delta\lambda_{eff}$ ($\times10^{-28}$ cm^3)	2.17	2.07	2.48
	$\sigma_e \times \tau_{rad}$ ($\times10^{-25}$ cm^2 s)	0.5562	12.55	29.8653
$0.07Sm^{3+}$	λ_p(nm)	567	617	651
	A_R (s^{-1})	88.95	642.21	629.01
	β_R (Radiative)	0.0653	0.4721	0.4624
	β_R (Experimental)	0.2044	0.2780	0.5175
	σ_e ($\times10^{-22}cm^2$)	0.6585	17.03	40.57
	$\sigma_e \times \Delta\lambda_{eff}$ ($\times10^{-28}$ cm^3)	2.31	2.34	2.84
	$\sigma_e \times \tau_{rad}$ ($\times10^{-25}$ cm^2 s)	0.4839	12.51	29.81
$0.1Sm^{3+}$	λ_p(nm)	567	617	651
	A_R (s^{-1})	99.42	750.40	787.25
	β_R (Radiative)	0.0607	0.4583	0.4808
	β_R (Experimental)	0.2289	0.3012	0.4697
	σ_e ($\times10^{-22}cm^2$)	0.6850	17.434	51.516
	$\sigma_e \times \Delta\lambda_{eff}$ ($\times10^{-28}$ cm^3)	2.5923	2.7434	3.5670
	$\sigma_e \times \tau_{rad}$ ($\times10^{-25}$ cm^2 s)	0.4185	10.6521	31.4762

The stimulated emission cross-section is determined by the expression [24]:

$$\sigma_e = \frac{\lambda_p^4 A_R(J'\rightarrow J)}{8\pi Cn^2\,\Delta\lambda_{eff}} \tag{17}$$

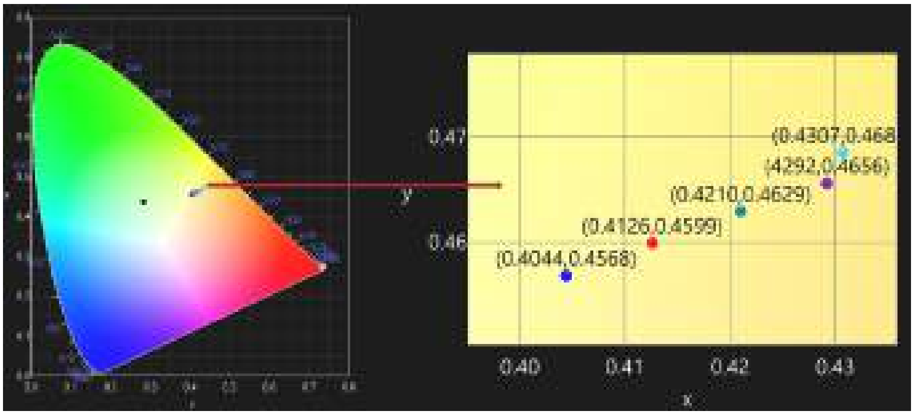

Fig. 7. CIE coordinates of $LiCa_2Mg_2V_3O_{12}$:xSm^{3+} phosphors.

Table 8
CIE, CRI and CCT values of $LiCa_2Mg_2V_3O_{12}$:xSm^{3+} phosphors.

Sm^{3+} (mol%)	CIE	CRI	CCT
0	(0.2832,0.4372)	57	6974
1	(0.4044,0.4568)	81	3957
3	(0.4126,0.4599)	81	3821
5	(0.4210,0.4629)	80	3691
7	(0.4292,0.4656)	82	3567
10	(0.4307,0.4685)	79	3560

Table 9
τ_{exp}, τ_{rad} and η values of $LiCa_2Mg_2V_3O_{12}$:xSm^{3+}phosphors.

Parameters	0.01Sm^{3+}	0.03Sm^{3+}	0.05Sm^{3+}	0.07Sm^{3+}	0.1Sm^{3+}
τ_{rad} (ms)	1.1180	0.9427	0.8326	0.7350	0.6110
τ_{exp} (ms)	0.8969	0.7443	0.6158	0.4794	0.3434
η	80.29	78.95	73.96	74.31	62.74

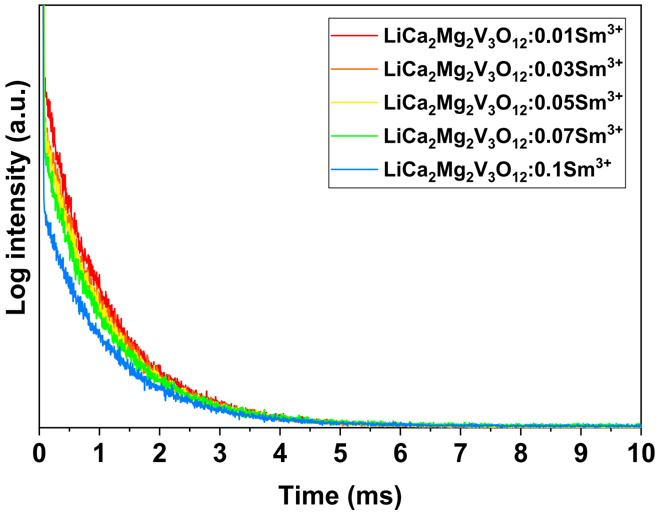

Fig. 8. Decay curve analysis of $LiCa_2Mg_2V_3O_{12}$:xSm^{3+}phosphors.

where λ_p is the value of peak wavelength and $\Delta\lambda_{eff}$ is the effective wavelength. The various radiative parameters of $LiCa_2Mg_2V_3O_{12}$:xSm^{3+} phosphors are consolidated in Table 7, where $\sigma_e \times \Delta\lambda_{eff}$ and $\sigma_e \times \tau_R$ values represent gain band width and optical gain respectively. Among the phosphors, the $^4G_{5/2}\rightarrow{}^6H_{9/2}$ transition of $LiCa_2Mg_2V_3O_{12}$:0.07Sm^{3+} phosphor have admirable properties of branching ratio (≥ 0.5), emission cross-section and optical gain. Thus, the synthesized phosphor is an apt candidate for lasing action [28,37].

The CIE color coordinates of phosphors monitored at an excitation wavelength of 338 nm is shown in Fig. 7. The color of phosphor shifts from green to yellow region with increase in Sm^{3+} concentration. The CIE color coordinates, correlated color temperature (CCT) and color rendering index (CRI) values are tabulated in Table 8. The Sm^{3+} doped phosphors have excellent CRI values (above 75) and exhibits admirable color appearance [23]. The CCT value of doped phosphors is less than 5000 K and is a warm light source. The internal quantum efficiency of optimum concentraion phosphor $LiCa_2Mg_2V_3O_{12}$:0.07Sm^{3+} is evaluated with respect to $BaSO_4$ refernce and is found to be 43.17% which is higher than the quauntum efficiency of $LiCa_3ZnV_3O_{12}$:Sm^{3+} (36.1 %) [5], $LiCa_2Mg_2V_3O_{12}$:Dy^{3+} (31.40%) [26], $LiCa_2SrMgV_3O_{12}$:Eu^{3+} (39.3%) [38] and $Ca_3LiZnV_3O_{12}$:Eu^{3+} (40.19%) phosphors [39]. Thus the phosphor can be utilized for the development of indoor lighting devices and LEDs [40].

The decay curve analysis of phosphors is performed (λ_{ex}=338 nm andλ_{em} = 651 nm) and is shown in Fig. 8. The curves can be well fitted by mono exponential function, as defined below [36]:

$$I(t) = A^{*}exp(-t/\tau) \tag{19}$$

where *I(t)* is the luminescence intensity at time *t*, *A* is the weight factor and τ is the luminescence life time. The lifetime of phosphors are evaluated to be 1.1180, 0.9427, 0.8326, 0.7350 and 0.6110 ms respectively. The lifetime decreases with increase in Sm^{3+} concentration and is attributed to the non-radiative energy transfer [36]. The radiative lifetime of phosphors calculated from Judd-Ofelt analysis is 0.8969, 0.7443, 0.6158, 0.4794 and 0.3434 ms respectively. The discrepancy between experimental lifetime (τ_{exp}) and radiative lifetime (τ_{rad}) is due to non-radiative relaxation process. The intrinsic quantum efficiency (η) is calculated from experimental to radiative lifetime using equation [41]:

$$\eta = \frac{\tau_{exp}}{\tau_{rad}} \times 100\% \tag{20}$$

The values of τ_{exp}, τ_{rad} and η are tabulated in Table 9. The phosphors have high quantum efficiency compared to other Sm^{3+} doped phosphors $Sr_{1.0}Ba_{2.0}B_6O_{12}$:0.5Sm^{3+} (66.38%) [28], $Sr_{0.5}Ca_{0.5}TiO_3$:Sm^{3+} (16.38%) [33] and Sm_2O_2S (73.2%) [41].

3.4. Thermo sensor application

The thermal response of $LiCa_2Mg_2V_3O_{12}$:0.07Sm^{3+} phosphor is explored to test the possible application in non-contact optical thermometry. The temperature dependent emission spectra of $LiCa_2Mg_2V_3O_{12}$:0.07Sm^{3+} phosphor in heating up and cooling down process from 80 K to 500 K are represented in Fig. 9**(a) & (b)** respectively. As the temperature increases the PL emission intensity shows a

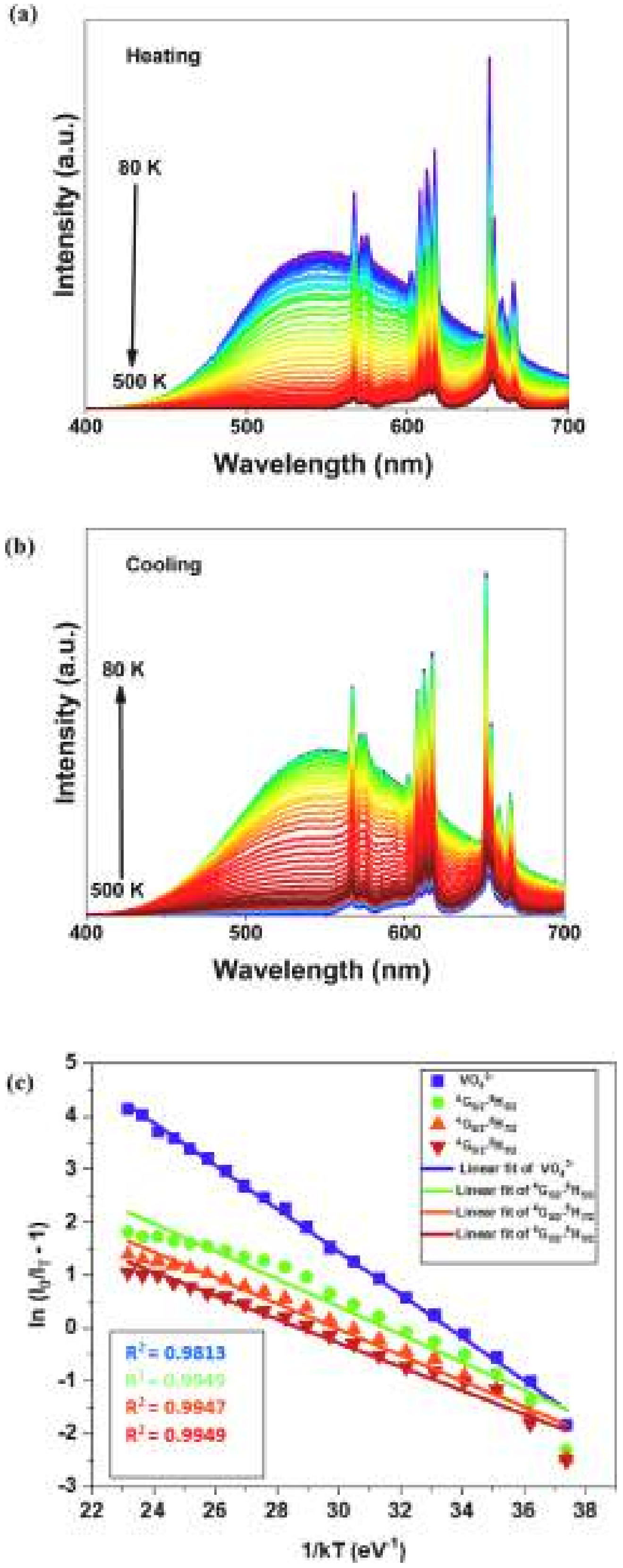

Fig. 9. FIR plot of $LiCa_2Mg_2V_3O_{12}$:0.07Sm^{3+} phosphor in **(a)** heating up and **(b)** cooling down process and (c) Arrhenius plot.

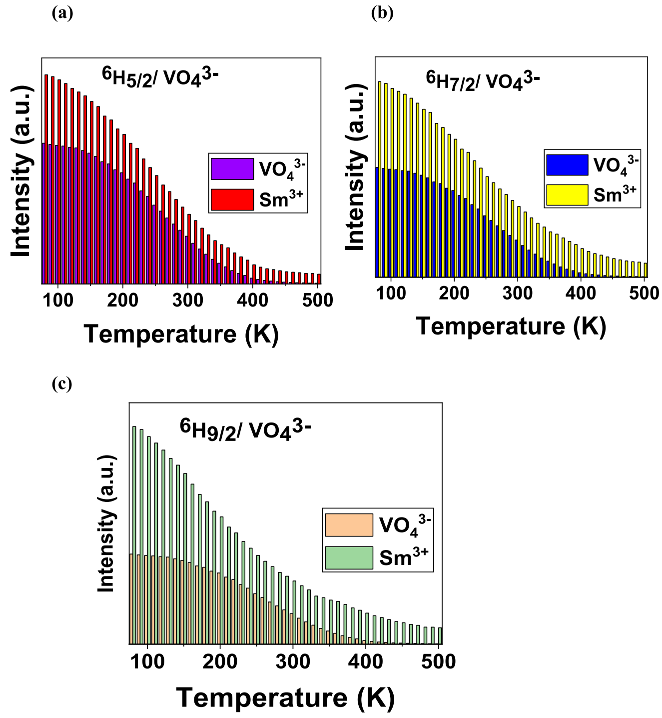

Fig. 10. The temperature dependent emission intensities of Sm^{3+} ion at **(a)** 567 nm ($^4G_{5/2}\rightarrow{}^6H_{5/2}$) **(b)** 617 nm ($^4G_{5/2}\rightarrow{}^6H_{7/2}$) and **(c)** 651 nm ($^4G_{5/2}\rightarrow{}^6H_{9/2}$) with respect to VO_4^{3-} group.

downward tendency due to the thermal quenching effect. From Fig. 9**(a)** it can be seen that the emission intensity of VO_4^{3-} group decreased sharply, while the Sm^{3+} shows moderate decrease in emission intensity with temperature. The relationship between PL emission intensity and temperature is given by Struck and Fonger theory and can be expressed as follows [5,13]:

$$I = \frac{I_0}{1 + Aexp(-\Delta E/kT)} \tag{21}$$

where I and I_0 are PL emission intensity at monitored temperature (T) and initial temperature respectively, ΔE refers to the activation energy, k represents the Boltzmann constant and A is a constant. Fig. 9**(c)** shows the Arrhenius plot of $1/kT$ against $\ln(I_0/I_T - 1)$, for VO_4^{3-} group and Sm^{3+} ($^4G_{5/2}\rightarrow{}^6H_{J\ =\ 5/2,\ 7/2,\ 9/2}$). The linear fitting of data points gives the activation energy responsible for thermal quenching and are estimated to be 0.4056, 0.2623, 0.2439 and 0.2243 eV respectively [5]. Since, the VO_4^{3-} group and Sm^{3+} shows diverse thermal response, the FIR values also show strong dependence to temperature. The FIR expression of Sm^{3+} ions to the VO_4^{3-} group can be given by the equation [13,18]:

$$FIR = \frac{I_{Sm^{3+}}}{I_{VO_4^{3-}}} = \frac{I_{0,Sm^{3+}}}{I_{0,VO_4^{3-}}}\frac{1 + A_{VO_4^{3-}}\exp(-\Delta E_{VO_4^{3-}}/kT)}{1 + A_{Sm^{3+}}\exp(-\Delta E_{Sm^{3+}}/kT)} \approx B + C\exp(-E/kT) \tag{22}$$

where B, C and E are constants related to the I_0, A and ΔE of Sm^{3+} ions to the VO_4^{3-} group. Fig. 10**(a)–(c)** shows the temperature dependent emission intensities of Sm^{3+} ion at 567 nm ($^4G_{5/2}\rightarrow{}^6H_{5/2}$), 617 nm ($^4G_{5/2}\rightarrow{}^6H_{7/2}$) and 651 ($^4G_{5/2}\rightarrow{}^6H_{9/2}$) nm with respect to VO_4^{3-} group. The diverse thermal response is utilized for the estimation of FIR values. The temperature dependent FIR values of $^4G_{5/2}\rightarrow{}^6H_J$ (J = 5/2, 7/2, 9/2) transition of Sm^{3+} to VO_4^{3-} group are displayed in Fig. 11**(a)–(c)**. The plot can be well fitted by Eq. (23) and the obtained values of B, C and E/k are listed in Table 10.

For each experimentally observed *FIR* value, the theoretical temperature of the sample can be determined using following equation [13]:

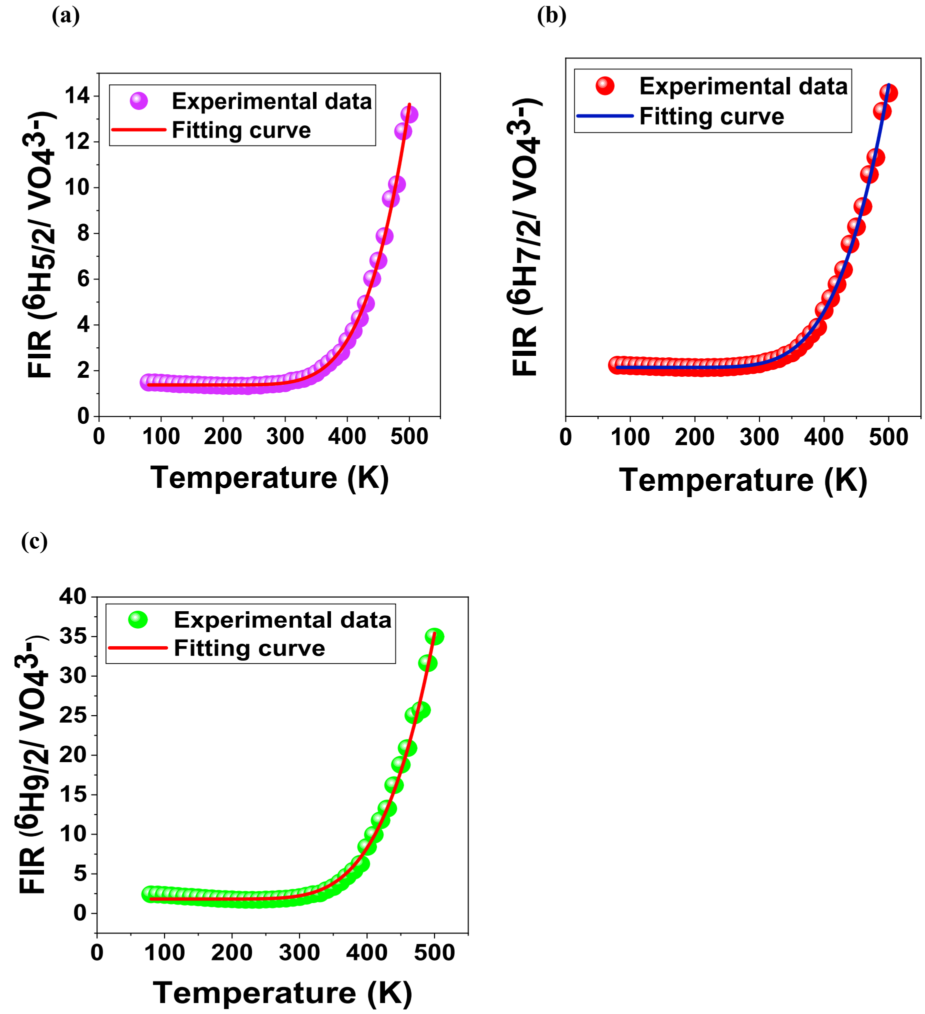

Fig. 11. The temperature dependent FIR plots of **(a)** $^4G_{5/2}\rightarrow{}^6H_{5/2}/\ VO_4^{3-}$ **(b)** $^4G_{5/2}\rightarrow{}^6H_{7/2}/\ VO_4^{3-}$ and **(c)** $^4G_{5/2}\rightarrow{}^6H_{9/2}/\ VO_4^{3-}$ combinations.

Table 10
Fitting curve values of *B*, *C* and *E*/*k*.

FIR	*B*	*C*	*E*/*k*
$^4G_{5/2}\rightarrow{}^6H_{5/2}/\ VO_4^{3-}$	1.3813	18575.05	3661.50
$^4G_{5/2}\rightarrow{}^6H_{7/2}/\ VO_4^{3-}$	1.5997	15204.77	3232.48
$^4G_{5/2}\rightarrow{}^6H_{9/2}/\ VO_4^{3-}$	1.8251	24419.03	3294.34

$$T = \left[\frac{1}{\ln C - \ln(FIR - B)}\right]\frac{E}{k} \tag{23}$$

The parameters in above equation have same meaning as described in Eq. (22). For each temperature, the difference between theoretical and experimental values are determined. From the differences the average value is calculated. The average difference between the theoretical and observed temperatures for $^4G_{5/2}\rightarrow{}^6H_{5/2}/\ VO_4^{3-}$, $^4G_{5/2}\rightarrow{}^6H_{7/2}/\ VO_4^{3-}$ and $^4G_{5/2}\rightarrow{}^6H_{9/2}/\ VO_4^{3-}$ are ± 0.82, ± 0.90 and ± 3.66 K respectively.

To get deeper insight into practical application of phosphor in thermal sensing, their absolute sensitivity (S_a) and relative sensitivity (S_r) are analysed. The S_a and S_r values are estimated by the following expressions [13,18]:

$$S_a = \frac{d(FIR)}{dT} = C\exp(-E/kT) \times (E/kT^2) \tag{24}$$

$$S_r = 100\% \times \frac{1}{FIR}\frac{d(FIR)}{dT} = 100\% \times \frac{C\exp(-E/kT)}{B + C\exp(-E/kT)} \times \frac{E}{kT^2} \tag{25}$$

The temperature dependence of S_a and S_r of $LiCa_2Mg_2V_3O_{12}$:0.07Sm^{3+} phosphor for the combinations $^6H_{5/2}/\ VO_4^{3-}$, $^6H_{7/2}/\ VO_4^{3-}$ and $^6H_{9/2}/\ VO_4^{3-}$ is shown in Fig. 12**(a)–(c)** respectively. It is noteworthy that all of the S_a values increase with rise in temperature and reaches maximum value at 500 K. The maximum S_a values for the combinations $^6H_{5/2}/\ VO_4^{3-}$, $^6H_{7/2}/\ VO_4^{3-}$ and $^6H_{9/2}/\ VO_4^{3-}$ are observed to be 0.1791, 0.3055 and 0.4418 K^{-1} respectively. The S_r values exhibit a different tendency with temperature, at first S_r increases, reaches a maximum value and then decreases with rise in temperature. For the combinations $^6H_{5/2}/\ VO_4^{3-}$, $^6H_{7/2}/\ VO_4^{3-}$ and $^6H_{9/2}/\ VO_4^{3-}$ the maximum S_r values are 1.4481% K^{-1} at 441.56 K, 1.5092% K^{-1} at 400 K and 1.6079% K^{-1} at 395.31 K respectively. The S_a and S_r values of $LiCa_2Mg_2V_3O_{12}$:0.07Sm^{3+} phosphor can be aptly tuned through adopting combinations $^6H_{5/2}/\ VO_4^{3-}$, $^6H_{7/2}/\ VO_4^{3-}$ and $^6H_{9/2}/\ VO_4^{3-}$ [12]. As compared to the S_a and S_r values of reported Sm^{3+} doped materials (Table 11**)**, the present system have efficient sensitivity in different modes of measurement. Thus, spectral mode selection is a reliable and convenient method to modulate optical thermometric characteristics of Sm^{3+} doped $LiCa_2Mg_2V_3O_{12}$ phosphor.

The thermal repeatability of the sample is further checked by evaluating the temperature dependence of FIR in heating and cooling process. Fig. 13**(a)** shows cycling test of $LiCa_2Mg_2V_3O_{12}$:0.07Sm^{3+} phosphor in $^6H_{9/2}/\ VO_4^{3-}$ combination to analyse the thermal stability. It is evident from the figure that the phosphor has good thermal repeatability and are highly reproducible.

In addition, temperature resolution (δT) of the phosphor can be calculated using expression [42]:

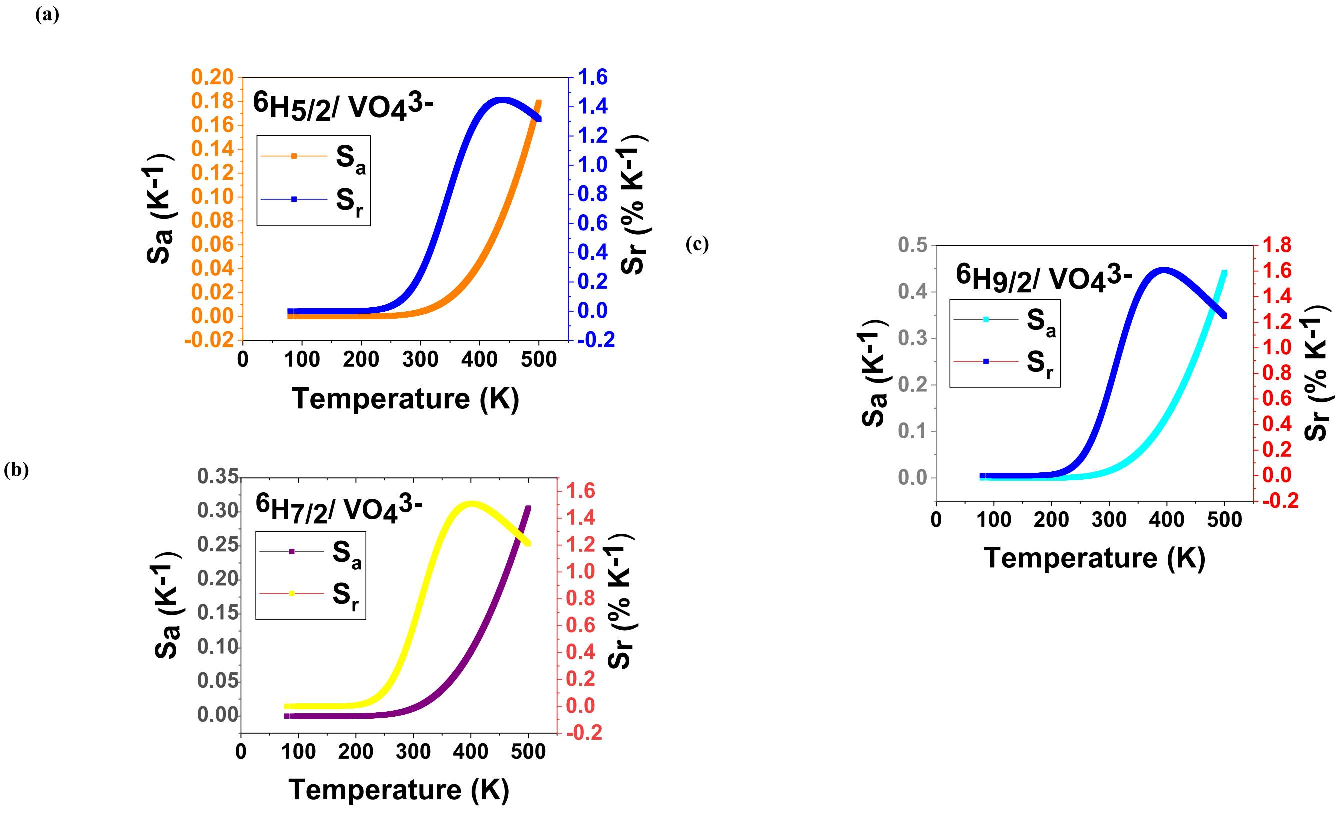

Fig. 12. The S_a and S_r plots of **(a)** $^6H_{5/2}/\ VO_4^{3-}$ **(b)** $^6H_{7/2}/\ VO_4^{3-}$ and **(c)** $^6H_{9/2}/\ VO_4^{3-}$ combinations.

Table 11
Comparative study of S_a and S_r values of Sm^{3+} doped materials.

Material	Temperature range (K)	*Sa*-max (K^{-1})	*Sr*-max (%K^{-1})	Ref.
$La_3NbO_7:Sm^{3+}$	303–483	0.05379 (483 K)	1.60 (303 K)	[43]
$Ca_2LaNbO_6:Sm^{3+}$	313–573	–	0.23 (353 K)	[44]
(65-x)TeO_2-20ZnF_2-12PbO-3Nb_2O_5-xSm_2O_3	300–725	0.0031 (700 K)	–	[45]
$YVO_4:Sm^{3+}$	299–466	0.00094	0.36 (466 K)	[46]
$Ca_2NaMg_2V_3O_{12}:Sm^{3+}$	303–503	0.0164 (503 K)	1.889 (463 K)	[15]
$SrB_4O_7:Sm^{2+}$	300–723	–	2.16 (500 K)	[47]
$LiCa_3ZnV_3O_{12}:Sm^{3+}$	303–463	0.25 (463 K)	1.8 (412 K)	[5]
$LiCa_2Mg_2V_3O_{12}:Sm^{3+}$	80–500	0.1791 (500 K) 0.3055 (500 K) 0.4418 (500 K)	1.4481 (441.56 K) 1.5092 (400 K) 1.6079 (395.31 K)	Present work

$$\delta T = \frac{1}{S_r}\frac{\delta FIR}{FIR} \tag{26}$$

where δFIR is the standard deviation of *FIR* in 3 consecutive cycles. Fig. 13**(b)** displays the calculated values of δT with respect to temperature for $^6H_{5/2}/\ VO_4^{3-}$, $^6H_{7/2}/\ VO_4^{3-}$ and $^6H_{9/2}/\ VO_4^{3-}$ combinations. The minimum δT of different spectral modes are 0.1633, 0.1677 and 0.1563 K respectively at 500 K. The phosphor has high temperature resolution in all spectral modes.

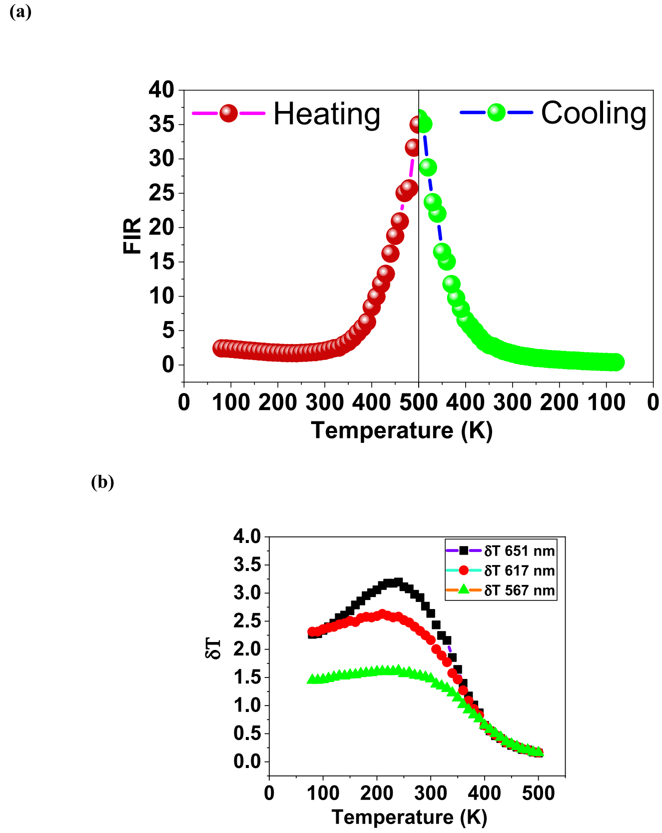

Fig. 13. **(a)** Cycling test of $LiCa_2Mg_2V_3O_{12}$:0.07Sm^{3+} phosphor and **(b)** δT with respect to temperature for $^6H_{5/2}/\ VO_4^{3-}$, $^6H_{7/2}/\ VO_4^{3-}$ and $^6H_{9/2}/\ VO_4^{3-}$ combinations.

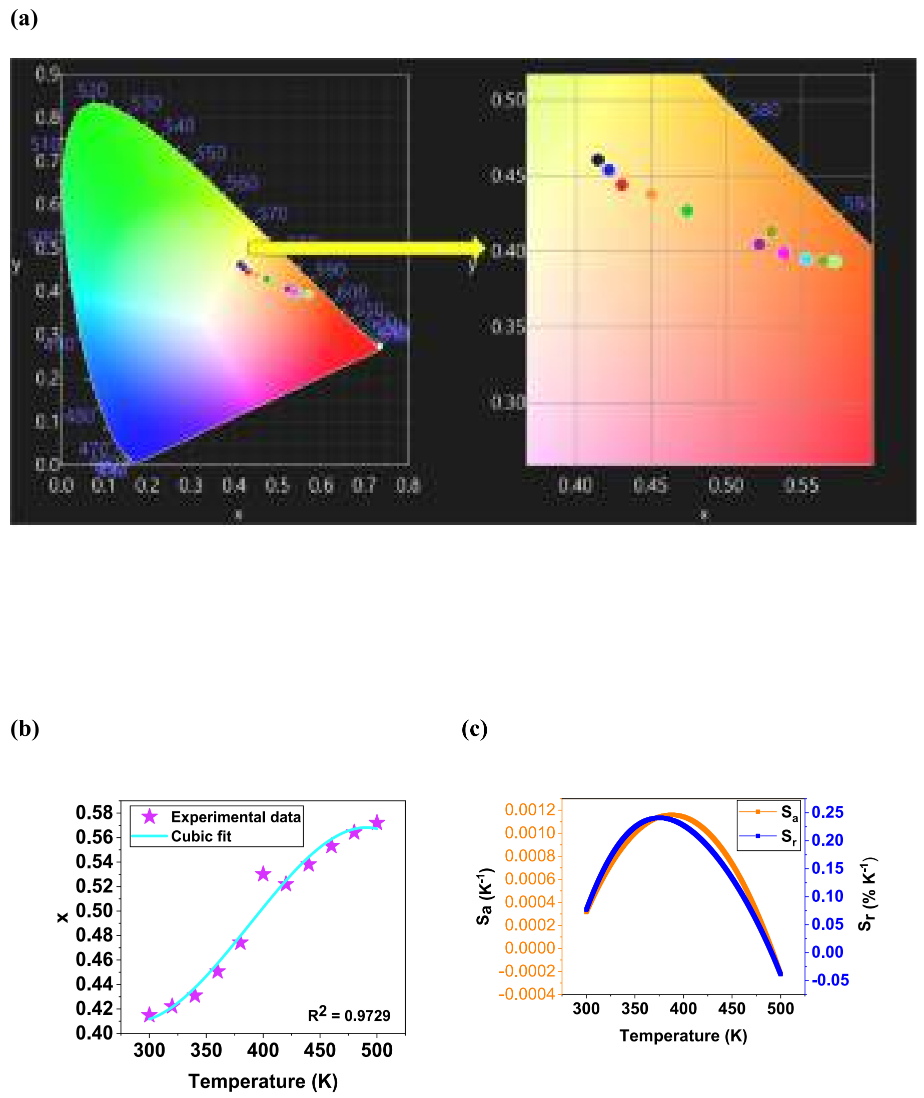

Fig. 14. **(a)** Temperature dependent CIE coordinates **(b)** CIE x-coordinate versus temperature and **(c)** $S_a(x)$ and $S_r(x)$ of $LiCa_2Mg_2V_3O_{12}$:0.07Sm^{3+} phosphor.

3.5. *Thermochromic properties*

Based on the diverse thermal response of VO_4^{3-} group and Sm^{3+} ion, the emission color of $LiCa_2Mg_2V_3O_{12}$:0.07Sm^{3+} phosphor can also vary with temperature. Fig. 14**(a)** shows the temperature dependent CIE coordinates of $LiCa_2Mg_2V_3O_{12}$:0.07Sm^{3+} phosphor under 338 nm excitation. The CIE coordinates of phosphor change from yellow to red as temperature rises from 300 K to 500 K. The color coordinate change can be evaluated by chromaticity shifts (Δs), as shown below [44]:

$$\Delta s = \sqrt{(u'_m - u'_0)^2 + (v'_m - v'_0)^2 + (w'_m - w'_0)^2} \quad (27)$$

where $u' = 4x/(3 - 2x + 12y)$, $v' = 9y/(3 - 2x + 12y)$ and $w' = 1 - u' - v'$,u'_0 and v'_0 are the chromaticity color coordinates in $u'v'$ uniform color space at 300 K, u'_m and v'_m are the chromaticity coordinates at 500 K and x and y are the values of CIE color coordinates. The Δs of $LiCa_2Mg_2V_3O_{12}$:0.07Sm^{3+} phosphor is calculated to be 0.1869 and is higher than the chromaticity shifts of $Cs_3GdGe_3O_9$:Er^{3+} (0.183), Zn_2GeO_4:Mn^{2+}/Eu^{3+} (0.052) [48], $KSr_4B_3O_9$: Ce^{3+}/Eu^{2+} (0.1652) [49] and $Lu_3Al_5O_{12}$:Ce^{3+}/Mn^{4+} (0.153) [50]. The higher value of Δs implies better color discrimination of the phosphor in high temperature environment. The present phosphor system find application in safety sign marking in high temperature conditions.

Fig. 14 **(b)** reveals that the CIE *x*-coordinate of phosphor is sensitive to temperature and this relationship can be used to detect temperature. The plot can be well fitted by the following equation [6]:

$$x = C_0 + C_1T + C_2T^2 + C_3T^3 \quad (28)$$

where C_0, C_1, C_2 and C_3 are coefficients. The $S_a(x)$ and $S_r(x)$ value can be further derived from Eqs. (25) and (26) by using *x*-function Eq. **(29)** in the place of FIR (Fig. 14**(c)**). The maximum value of $S_a(x)$ and $S_r(x)$ are 0.0011 K^{-1} (371 K) and 0.2407% K^{-1} (391 K) respectively.

4. Conclusions

A novel Sm^{3+} doped $LiCa_2Mg_2V_3O_{12}$ phosphors have been synthesized by solid state method. The PXRD study confirms the cubic phase (*Ia-3d*) of phosphor. The nephelauxetic ratio and bonding parameter estimated from UV–VIS-NIR absorption spectra demonstrates the covalence of Sm in $LiCa_2Mg_2V_3O_{12}$ host. The J-O parameters calculated from absorption spectra exhibit $\Omega_2 > \Omega_4 > \Omega_6$ tendency, which further confirms the covalence of bond. The PL spectra of Sm^{3+} doped $LiCa_2Mg_2V_3O_{12}$ phosphors monitored at 338 nm exhibit emissions of both VO_4^{3-} (513 nm) and Sm^{3+} (567, 617 and 651 nm). The emission shows concentration quenching at 7 mol% and is due to the dipole–dipole interaction. The radiative parameters are estimated from emission spectra and the higher branching ratio, quantum efficiency, emission cross section and optical gain elucidates the lasing application of phosphors. The CIE, CCT and CRI values indicate that the phosphors can be employed to develop LEDs and display devices. The temperature dependent PL spectra of phosphor analysed by FIR method shows that using spectral mode selection ultra-high sensitive thermo sensors can be developed. For the combinations $^6H_{5/2}$/ VO_4^{3-}, $^6H_{7/2}$/ VO_4^{3-} and $^6H_{9/2}$/ VO_4^3 the S_a values are evaluated to be 0.1791, 0.3055 and 0.4418 K^{-1} respectively and the S_r values are found to be 1.4481, 1.5092 and 1.6079% K^{-1} respectively. The phosphors also possess high temperature resolution in each spectral mode. The thermochromic properties shows better chromaticity shift ($\Delta s = 0.1869$) and the color changes from yellow to red region (300–500 K). This implies the safety sign marking application of phosphor. The CIE coordinates used for the determination of sensitivity displays $S_a(x)$ and $S_r(x)$ values 0.0011 K^{-1} and 0.2407% K^{-1} respectively. Hence, the above results suggest that present phosphor is an apt candidate for multifunctional applications.

CRediT authorship contribution statement

R. Raji: Conceptualization, Methodology, Investigation, Validation, Formal analysis, Writing - original draft. **P.S. Anjana:** Supervision, Resources, Formal analysis, Writing - review & editing. **N. Gopakumar:** Supervision, Resources, Formal analysis, Writing - review & editing.

Declaration of competing interest

The authors declare that they have no known competing financial interests or personal relationships that could have appeared to influence the work reported in this paper.

Data availability

Data will be made available on request.

Acknowledgements

One of the authors acknowledges University of Kerala for financial support under University Junior Research Fellowship. The authors are thankful to CLIF, University of Kerala and SAIF, M.G University, Kerala for providing characterization facility.

References

[1] J.Q. Chen, J.Y. Chen, W.N. Zhang, S.J. Xu, L.P. Chen, H. Guo, Three-mode optical thermometer based on Ca3LiMgV3O12:Sm3+ phosphors, Ceram. Int. 49 (2023), https://doi.org/10.1016/j.ceramint.2023.01.223.

[2] Y.C. Jiang, Y. Tong, S.Y.Z. Chen, W.N. Zhang, F.F. Hu, R.F. Wei, H. Guo, A three-mode self-referenced optical thermometry based on up-conversion luminescence of Ca2MgWO6:Er3+, Yb3+ phosphors, Chem. Eng. J. 413 (2021) 127470, https://doi.org/10.1016/j.cej.2020.127470.

[3] X. Shi, M. Zhang, X. Lu, Q. Mao, L. Pei, H. Yu, J. Zhang, M. Liu, J. Zhong, High sensitivity and multicolor tunable optical thermometry in Bi3+/Eu3+ co-doped Ca2Sb2O7 phosphors, Mater. Today Chem. 27 (2023), https://doi.org/10.1016/j.mtchem.2022.101264.

[4] G. Li, G. Li, Q. Mao, L. Pei, H. Yu, M. Liu, L. Chu, J. Zhong, Efficient luminescence lifetime thermometry with enhanced Mn4+-activated BaLaCa1−xMgxSbO6 red phosphors, Chem. Eng. J. 430 (2022), https://doi.org/10.1016/j.cej.2021.132923.

[5] H. Guo, B. Devakumar, R. Vijayakumar, P. Du, X. Huang, A novel Sm3+ singly doped LiCa3ZnV3O12 phosphor: a potential luminescent material for multifunctional applications, RSC Adv. 8 (2018) 33403–33413, https://doi.org/10.1039/c8ra07329e.

[6] J.Y. Chen, J.Q. Chen, L.J. Li, W.N. Zhang, L.P. Chen, H. Guo, A four-mode high-sensitive optical thermometer based on Ca3LiZnV3O12:Sm3+ phosphors, Mater. Today Chem. 29 (2023), https://doi.org/10.1016/j.mtchem.2023.101409.

[7] S.J. Xu, J.H. Lei, L.J. Li, J.Y. Chen, L.P. Chen, H. Guo, Dual-mode optical thermometry of Sr2YNbO6:Bi3+, Eu3+ phosphors designed by response surface methodology, J. Lumin. 255 (2023), https://doi.org/10.1016/j.jlumin.2022.119615.

[8] Y. Hua, T. Wang, J.S. Yu, P. Du, Tailoring of strong orange-red-emitting materials for luminescence lifetime thermometry, anti-counterfeiting, and solid-state lighting applications, Mater. Today Chem. 25 (2022), https://doi.org/10.1016/j.mtchem.2022.100945.

[9] H. Zhang, Z. Gao, G. Li, Y. Zhu, S. Liu, K. Li, Y. Liang, A ratiometric optical thermometer with multi-color emission and high sensitivity based on double perovskite LaMg0.402Nb0.598O3: Pr3+ thermochromic phosphors, Chem. Eng. J. 380 (2020), https://doi.org/10.1016/j.cej.2019.122491.

[10] Y. Hua, X. Qiu, C. Sonne, R.J.C. Brown, K.H. Kim, Construction of novel luminescent thermometers based on dual-emission centers of rare-earth and bismuth ions, Chemosphere 303 (2022), https://doi.org/10.1016/j.chemosphere.2022.135150.

[11] L. Mukhopadhyay, V.K. Rai, Investigation of photoluminescence properties, Judd-Ofelt analysis, luminescence nanothermometry and optical heating behaviour of Er3+/Eu3+/Yb3+:NaZnPO4 nanophosphors, New J. Chem. 42 (2018) 13122–13134, https://doi.org/10.1039/c8nj02320d.

[12] P. Du, Y. Hou, W. Li, L. Luo, Ultra-high sensitivity of multicolor Sm3+-doped LiSrVO4phosphors for contactless optical thermometers, Dalt. Trans. 49 (2020) 10224–10231, https://doi.org/10.1039/d0dt01907k.

[13] P. Du, Y. Hua, J.S. Yu, Energy transfer from VO43− group to Sm3+ ions in Ba3 (VO4)2:3xSm3+ microparticles: A bifunctional platform for simultaneous optical thermometer and safety sign, Chem. Eng. J. 352 (2018) 352–359, https://doi.org/10.1016/j.cej.2018.07.019.

[14] Q. Ma, Q. Liu, M. Wu, Y. Liu, R. Wang, R. Zhou, Y. Xu, H. Wei, R. Mi, X. Min, L. Mei, Z. Huang, B. Ma, Eu3+-doped La2(MoO4)3 phosphor for achieving accurate temperature measurement and non-contact optical thermometers, Ceram. Int. 49 (2023), https://doi.org/10.1016/j.ceramint.2022.10.345.

[15] H. Zhou, N. Guo, X. Lü, Y. Ding, L. Wang, R. Ouyang, B. Shao, Ratiometric and colorimetric fluorescence temperature sensing properties of trivalent europium or samarium doped self-activated vanadate dual emitting phosphors, J. Lumin. 217 (2020) 116758, https://doi.org/10.1016/j.jlumin.2019.116758.

[16] H. Zhou, N. Guo, Q. Liang, Y. Ding, Y. Pan, Y. Song, R. Ouyang, Y. Miao, B. Shao, Novel ratiometric optical thermometry based on dual luminescent centers from europium doped $LiCa_3MgV_3O_{12}$ phosphor, Ceram. Int. 45 (2019) 16651–16657, https://doi.org/10.1016/j.ceramint.2019.05.207.

[17] J. Fu, L. Zhou, Y. Chen, J. Lin, R. Ye, D. Deng, L. Chen, S. Xu, Dual-mode optical thermometry based on Bi3+/Sm3+ co-activated BaGd2O4 phosphor with tunable sensitivity, J. Alloys Compd. 897 (2022), https://doi.org/10.1016/j.jallcom.2021.163034.

[18] T. Hasegawa, Y. Abe, A. Koizumi, T. Ueda, K. Toda, M. Sato, Bluish-White Luminescence in Rare-Earth-Free Vanadate Garnet Phosphors: Structural Characterization of LiCa3MV3O12 (M = Zn and Mg), Inorg. Chem. 57 (2018) 857–866, https://doi.org/10.1021/acs.inorgchem.7b02820.

[19] X. Huang, H. Guo, LiCa3MgV3O12:Sm3+: A new high-efficiency white-emitting phosphor, Ceram. Int. 44 (2018) 10340–10344, https://doi.org/10.1016/j.ceramint.2018.03.043.

[20] X. Zhang, Z. Zhu, Z. Guo, Z. Sun, L. Zhou, Z. chao Wu, Synthesis, structure and luminescent properties of Eu3+ doped Ca3LiMgV3O12 color-tunable phosphor, Ceram. Int. 44 (2018) 16514–16521, https://doi.org/10.1016/j.ceramint.2018.06.069.

[21] J. Zhou, X. Huang, J. You, B. Wang, H. Chen, Q. Wu, Synthesis, energy transfer and multicolor luminescent property of Eu3+-doped LiCa2Mg2V3O12 phosphors for warm white light-emitting diodes, Ceram. Int. 45 (2019) 13832–13837, https://doi.org/10.1016/j.ceramint.2019.04.080.

[22] K. Thomas, D. Alexander, S. Sisira, L.A. Jacob, P.R. Biju, N.V. Unnikrishnan, M. A. Ittyachen, C. Joseph, Sm3+ doped tetragonal lanthanum molybdate: A novel host sensitized reddish orange emitting nanophosphor, J. Lumin. 211 (2019) 284–291, https://doi.org/10.1016/j.jlumin.2019.03.045.

[23] T. Krishnapriya, A. Jose, T. Anna Jose, C. Joseph, N.V. Unnikrishnan, P.R. Biju, Luminescent kinetics of Dy3+ doped CaZn2(PO4)2 phosphors for white light emitting applications, Adv. Powder Technol. 32 (2021) 1023–1032, https://doi.org/10.1016/j.apt.2021.02.003.

[24] R. Nagaraj, V. Rajagopal, A. Raja, S. Ranjith, Influence of Dy3+ ion concentration on photoluminescence and energy transfer mechanism of promising KBaScSi3O9 phosphors for warm white LEDs, Spectrochim. Acta - Part A Mol. Biomol. Spectrosc. 264 (2022) 120212, https://doi.org/10.1016/j.saa.2021.120212.

[25] C. Manjunath, M.S. Rudresha, B.M. Walsh, R. Hari Krishna, B.S. Panigrahi, B. M. Nagabhushana, Optical absorption intensity analysis using Judd-Ofelt theory and photoluminescence investigation of orange-red Sr2SiO4: Sm3+nanopigments, Dye. Pigment. 148 (2018) 118–129, https://doi.org/10.1016/j.dyepig.2017.08.036.

[26] R. Raji, P.S. Anjana, N. Gopakumar, An insight into Judd-Ofelt analysis and non-contact optical thermometry of LiCa2Mg2V3O12: Dy3+ phosphors for multifunctional applications, Opt. Mater. (amst). 145 (2023), https://doi.org/10.1016/j.optmat.2023.114393.

[27] W.T. Carnall, P.R. Fields, K. Rajnak, Electronic energy levels of the trivalent lanthanide aquo ions. IV. Eu 8+, J. Chem. Phys. 49 (1968) 4424–4442, https://doi.org/10.1063/1.1669893.

[28] S. Thomas, R. George, N. Qamhieh, K.G. Gopchandran, S.T. Mahmoud, A. Quatela, Sm3+-doped strontium barium borate phosphor for white light emission: Spectroscopic properties and Judd-Ofelt analysis, Spectrochim. Acta - Part A Mol. Biomol. Spectrosc. 248 (2021) 119187, https://doi.org/10.1016/j.saa.2020.119187.

[29] G. Jyothi, L.S. Kumari, K.G. Gopchandran, White emitting Dy3+ activated perovskite titanates and energy transfer by Eu3+ codoping, Ceram. Int. 43 (2017) 12044–12056, https://doi.org/10.1016/j.ceramint.2017.06.058.

[30] V. Vidyadharan, E. Sreeja, S.K. Jose, C. Joseph, N.V. Unnikrishnan, P.R. Biju, Spectroscopic and photoluminescence characterization of Dy3+ in Sr0.5Ca0.5TiO3 phosphor, Luminescence 31 (2016) 202–209, https://doi.org/10.1002/bio.2946.

[31] S.R. Yashodha, N. Dhananjaya, C. Manjunath, Synthesis and photoluminescence properties of Sm3+ doped LaOCl phosphor with reddish orange emission and it's Judd- Ofelt analysis, Mater. Res. Express 7 (2020), https://doi.org/10.1088/2053-1591/ab57a6.

[32] S. Thomas, S.N. Rasool, M. Rathaiah, V. Venkatramu, C. Joseph, N. V. Unnikrishnan, Spectroscopic and dielectric studies of Sm3+ ions in lithium zinc borate glasses, J. Non. Cryst. Solids 376 (2013) 106–116, https://doi.org/10.1016/j.jnoncrysol.2013.05.022.

[33] V. Vidyadharan, M.P. Remya, S. Gopi, S. Thomas, C. Joseph, N.V. Unnikrishnan, P. R. Biju, Synthesis and luminescence characterization of Sr0.5Ca0.5TiO3:Sm3+ phosphor, Spectrochim. Acta - Part A Mol. Biomol. Spectrosc. 150 (2015) 419–429, https://doi.org/10.1016/j.saa.2015.05.054.

[34] Z. Wu, B. Chen, X. Li, J. Zhang, J. Sun, H. Zhong, H. Zheng, L. Tong, H. Xia, Optical transition properties, energy transfer mechanism and luminescent thermal stability of Sm3+-doped silicate glasses, J. Alloys Compd. 663 (2016) 545–551, https://doi.org/10.1016/j.jallcom.2015.12.140.

[35] S. Mohan, S. Kaur, P. Kaur, D.P. Singh, Spectroscopic investigations of Sm3+-doped lead alumino-borate glasses containing zinc, lithium and barium oxides, J. Alloys Compd. 763 (2018) 486–495, https://doi.org/10.1016/j.jallcom.2018.05.319.

[36] R. Cao, X. Wang, Y. Jiao, X. Ouyang, S. Guo, P. Liu, H. Ao, C. Cao, A single-phase NaCa2Mg2V3O12:Sm3+ phosphor: Synthesis, energy transfer, and luminescence properties, J. Lumin. 212 (2019) 23–28, https://doi.org/10.1016/j.jlumin.2019.04.017.

[37] R. Nagaraj, R. Vijayakumar, N. Karunagaran, A. Raja, S. Ranjith, Realizing enhanced down-conversion photoluminescence and Judd-Ofelt parameters of novel reddish-orange emitting KBaScSi3O9:xSm3+ silicate phosphors, Mater. Sci. Eng. B Solid-State Mater. Adv. Technol. 276 (2022), https://doi.org/10.1016/j.mseb.2021.115537.

[38] H. Chen, J. Zhou, H. Zhang, Z. Hu, Broad-band emission and color tuning of Eu3+-doped LiCa2SrMgV3O12 phosphors for warm white light-emitting diodes, Opt. Mater. (amst) 89 (2019) 132–137, https://doi.org/10.1016/j.optmat.2019.01.012.

[39] X. Zhang, Z. Zhu, Z. Sun, Z. Guo, J. Zhang, Host-sensitized color-tunable luminescence properties of self-activated and Eu3+-doped Ca3LiZnV3O12 phosphors, J. Lumin. 203 (2018) 735–740, https://doi.org/10.1016/j.jlumin.2018.07.030.

[40] C. Kumari, J. Manam, S.K. Sharma, Study of photoluminescence behaviors and Judd-Ofelt analysis of Eu3+ doped double perovskite Ba2GdSbO6 phosphor for highly pure and strong red-light generation, J. Lumin. 263 (2023) 119983, https://doi.org/10.1016/j.jlumin.2023.119983.

[41] R.V. Rodrigues, E.J.B. Marciniak, P.C.M. Muri, R.C.S. Cruz, A.S. Oliveira, L. U. Borges, A.A.L. Khan, J.R. Marins, W.S. Matos, Optical properties and Judd-Ofelt analysis of Sm3+ ions in Sm2O2S: Reddish-orange emission and thermal stability, Opt. Mater. (amst). 107 (2020) 110160, https://doi.org/10.1016/j.optmat.2020.110160.

[42] Y. Luo, D. Zhang, S. Xu, L. Li, L. Chen, H. Guo, Optical thermometry based on Bi3+, Ln3+ co-doped YNbO4 (Ln = Dy, Eu) phosphors, J. Lumin. 257 (2023) 119780, https://doi.org/10.1016/j.jlumin.2023.119780.

[43] Y. Hua, J.U. Kim, J.S. Yu, Charge transfer band excitation of La3NbO7:Sm3+ phosphors induced abnormal thermal quenching toward high-sensitivity thermometers, J. Am. Ceram. Soc. 104 (2021) 4065–4074, https://doi.org/10.1111/jace.17805.

[44] A. Zhang, Z. Sun, M. Jia, Z. Fu, B.C. Choi, J.H. Jeong, S.H. Park, Sm3+-doped niobate orange-red phosphors with a double-perovskite structure for plant cultivation and temperature sensing, J. Alloys Compd. 889 (2022) 161671, https://doi.org/10.1016/j.jallcom.2021.161671.

[45] B. Klimesz, R. Lisiecki, W. Ryba-Romanowski, Sm3+-doped oxyfluorotellurite glasses - spectroscopic, luminescence and temperature sensor properties, J. Alloys Compd. 788 (2019) 658–665, https://doi.org/10.1016/j.jallcom.2019.02.215.

[46] I.E. Kolesnikov, E.V. Golyeva, M.A. Kurochkin, E.Y. Kolesnikov, E. Lähderanta, Concentration series of Sm3+-doped YVO4 nanoparticles: Structural, luminescence and thermal properties, J. Lumin. 219 (2020) 116946, https://doi.org/10.1016/j.jlumin.2019.116946.

[47] Z. Cao, X. Wei, L. Zhao, Y. Chen, M. Yin, Investigation of SrB4O7:Sm2+ as a Multimode Temperature Sensor with High Sensitivity, ACS Appl. Mater. Interfaces 8 (2016) 34546–34551, https://doi.org/10.1021/acsami.6b10917.

[48] H. Yao, Y. Zhang, Y. Xu, Dopant concentration-dependent morphological evolution of Zn2GeO4:Mn2+/Eu3+ phosphor and optical temperature sensing performance, J. Alloys Compd. 770 (2019) 149–157, https://doi.org/10.1016/j.jallcom.2018.08.105.

[49] Q. Lv, X. Ma, Y. Dong, Y. Li, B. Shao, C. Wang, S. Yang, C. Wang, Ratiometric optical thermometer with high-sensitive temperature sensing based on tunable luminescence of Ce3+-Eu2+ in KSr4B3O9 phosphors, Adv. Powder Technol. 33 (2022), https://doi.org/10.1016/j.apt.2022.103769.

[50] Y. Chen, J. He, X. Zhang, M. Rong, Z. Xia, J. Wang, Z.Q. Liu, Dual-Mode Optical Thermometry Design in Lu3Al5O12:Ce3+/Mn4+ Phosphor, Inorg. Chem. 59 (2020) 1383–1392, https://doi.org/10.1021/acs.inorgchem.9b03107.